参赛学生姓名：Megan Li

中学：郑州中学

省份：河南省

国家/地区：中国

指导老师姓名：宋荣斌、李朝辉

指导老师单位：郑州大学

论文题目：Metal Ion-Mediated Modulation of Human Chorionic Gonadotropin Immunoactivity on Commercial Pregnancy Test Strips for PFOS Point-of-Care Testing

2026 Si-Yau High School Science Award
仅用于2026丘成桐中学科学奖论文公示

论文题目：Metal Ion-Mediated Modulation of Human Chorionic Gonadotropin Immunoactivity on Commercial Pregnancy Test Strips for PFOS Point-of-Care Testing
作者：Megan Li, 郑州中学

Abstract

Perfluorooctanesulfonic acid (PFOS) is a persistent, bioaccumulative, and toxic environmental pollutant, yet its point-of-care testing (POCT) remains challenging due to the reliance on costly instruments and complex pretreatments in conventional methods. Although commercial pregnancy test strip (PTS)-based strategies are appealing for POCT, they are hindered by the laborious covalent conjugation of human chorionic gonadotropin (hCG) with DNA, which may block the critical recognition sites of hCG. Herein, this study proposes a non-conjugation signal transduction strategy based on metal ion-mediated modulation of hCG immunoactivity. Our design features a magnetic nucleic acid probe that specifically recognizes PFOS. The recognition probe was constructed by first immobilizing SH-labeled complementary DNA (cDNA) onto Fe_3O_4@Au via Au-S bonds and then hybridizing the aptamer to the cDNA (designated Fe_3O_4@Au@cDNA@Apt). In the presence of PFOS, the aptamer is released from the recognition probe and chelates zirconium ion (Zr^{4+}), thereby inhibiting the binding of Zr^{4+} to hCG. As a result, free hCG can be captured by the antibody on the test (T) line, generating a positive signal. Conversely, in the absence of PFOS, free Zr^{4+} binds directly to hCG, blocking antibody recognition and producing a negative signal. By integrating aptamer-functionalized magnetic enrichment (1000-fold) with the PTS sensor, PFOS was quantified to a limit of 10 nM (~5 ppb) with a linear range from 10 to 400 nM. To further improve the portability of the detection, a portable microfluidic chip was constructed, enabling effective PFOS detection in real water samples. This work presents a low-cost, field-deployable, and user-friendly POCT platform for emerging organic pollutants, bridging innovative sensing strategies with a mature commercial device.

Keywords

Perfluorooctanesulfonic acid; Point-of-care testing; Pregnancy test strip; Aptamer; Competitive response

2026 S.T. Yau High School Science Award
仅用于2026丘成桐中学科学奖公示

Contents

Abstract 2

Keywords 2

1. Introduction 5

1.1 Background 5

1.2 Research Status 6

1.3 Objectives and Innovations 12

2. Methods 13

2.1 Chemicals and Materials 13

2.2 Apparatus 14

2.3 Sequence Optimization and Affinity Evaluation of the PFOS-Specific Aptamer and Its Complementary DNA 15

2.4 Fabrication of the Fe_3O_4@Au@cDNA@Apt Magnetic Recognition Probes and Fe_3O_4@Au@Apt Magnetic Enrichment Probes 15

2.5 Quantitative Detection of PFOS 16

2.6 Investigation of Signal Transduction Mechanism Based on hCG Immunoactivity Regulation 17

2.7 Magnetic Enrichment of PFOS 18

2.8 Development of the Microfluidic Chip 18

2.9 Collection and Pretreatment of Environmental Water Samples 19

2.10 Integrated Detection of Environmental Pollutants Using Magnetic Enrichment Coupled with the Microfluidic Chip 20

3. Results and Discussion 20

3.1. Characterization of Fe_3O_4@Au@cDNA@Apt Magnetic Recognition Probes. 20

3.2. Feasibility of the Sensing Strategy and Mechanism of Zr^{4+}-Regulated hCG Immunoactivity 23

3.3. Analytical Performance of the PTS Sensor for PFOS 25

3.4. Integrated Detection of Environmental Pollutants via Enrichment-PTS-Microfluidic Chip Sensor 30

2026 S.-T. Yau High School Science Award
仅用于2026日成科中学科学论文公示

4. Conclusions 32
Acknowledgments 33
References 35

2026 S.-T. Yau High School Science Award
仅用于2026丘成桐中学科学奖论文公示

1. Introduction

1.1 Background

Perfluorooctanesulfonic acid (PFOS) is one of the most representative persistent organic pollutants among per- and polyfluoroalkyl substances. It possesses a distinctive molecular structure consisting of a hydrophobic fluorocarbon chain of eight perfluorinated carbon atoms and a terminal sulfonate group (SO_3^-). The carbon-fluorine (C-F) bonds in the structure exhibit exceptional chemical and thermodynamic stability, rendering PFOS highly resistant to chemical and microbial degradation and existing predominantly in anionic form in aqueous environments. In fact, also known as a "forever chemical", PFOS persists in water, soil, air, and other environmental media for extended periods [1]. Furthermore, the unique perfluorinated structure imparts excellent surface activity and physicochemical stability, leading to its extensive historical use in both industrial production and consumer products, including firefighting foam additives, non-stick coating materials, textile stain repellents, industrial lubricants, and functional auxiliaries in electroplating, semiconductor manufacturing, and flame-retardant production [2].

PFOS enters the environment via multiple pathways, such as industrial discharge, wastewater, and landfill leachate, and subsequently accumulates in water bodies, soil, and biota (Fig. 1.1) [3]. PFOS presents prominent bioaccumulation potential and undergoes trophic biomagnification along food chains, thereby exacerbating ecological risks at higher trophic levels. The favorable water solubility and strong capacity for long-range atmospheric transport further facilitate its transboundary diffusion through the global hydrological cycle. Therefore, PFOS has been widely detected in environmental media and organisms even in remote uninhabited regions such as polar areas. Moreover, PFOS exhibits considerable biological toxicity. For instance, chronic PFOS exposure can cause liver damage, immune suppression, and reproductive and developmental toxicity, while significantly raising the risk of liver, thyroid, and other cancers, posing persistent and irreversible threats to ecosystems and human health [4,5]. Given such extraordinary environmental persistence, global mobility, bioaccumulation

2026 S.-T. Yau High School Science Award
仅用于2026丘成桐中学科学奖论文公示

propensity, and toxicological hazards, PFOS has been officially listed as a priority-controlled substance under the Stockholm Convention [6]. Therefore, accurate and efficient PFOS detection is essential for characterizing its environmental concentrations, distribution, and migration, thereby enabling timely risk warning and the protection of ecological security and human health.

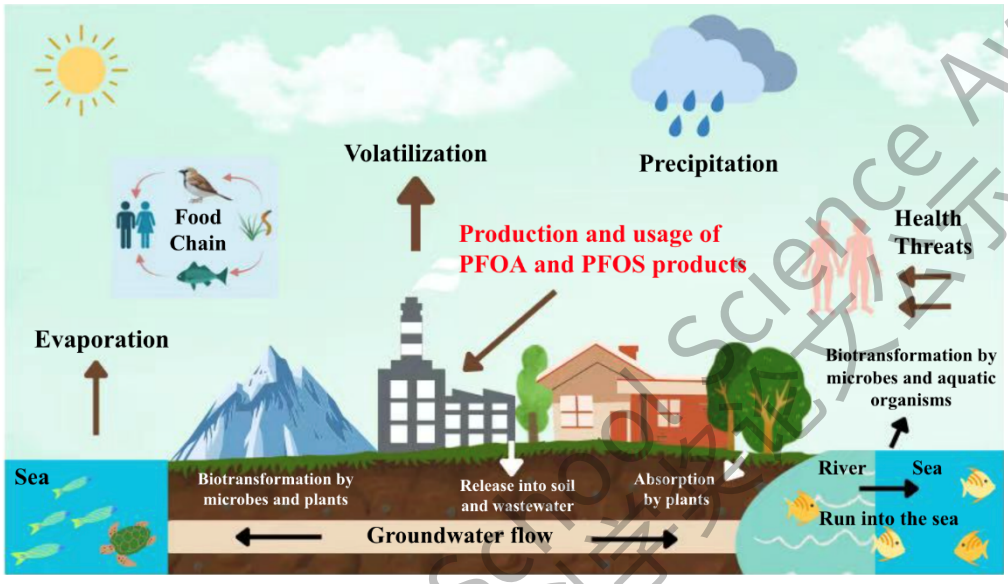


Figure 1.1. Environmental occurrence, transformation, and fate of PFOS.

1.2 Research Status

Conventional analytical strategies for PFOS mainly refer to chromatograph-mass spectrometry hyphenated techniques such as LC/MS and HPLC-MS/MS. Characterized by high selectivity and favorable quantitative performance, these methods achieve detection limits at low ppt level [7-9], thereby being formulated as standard analytical approaches for PFOS determination. Although accurate and definitive quantitative data can be obtained via these instrumental methods, their high equipment cost, requirement for skilled operators, and long testing time restrict their application in on-site and real-time monitoring. These inherent limitations highlight the urgent necessity to develop user-friendly, low-cost and highly-sensitive detection strategies for PFOS.

1.2.1 Electrochemical Detection Technology for PFOS

Electrochemical sensing is a technique that detects and quantifies targets by monitoring redox-induced electrochemical signals (e.g., current, potential, or impedance) at the electrode surface. It is worth noting that PFOS is electrochemically

2026 S.-T. Yau High School Science Award
仅用于2026丘成桐中学科学奖公示

inert, making it unsuitable for direct electrochemical detection. Consequently, current electrochemical methods for PFOS detection predominantly rely on indirect signal transduction mechanisms. The primary strategies include surfactant effect-based bubble nucleation assays [10,11], molecularly imprinted polymer (MIP)-modified electrodes [12,13], and nanomaterial-enhanced electrochemical biosensors [14]. These approaches aim to overcome the challenges associated with trace PFOS detection in complex environmental conditions by improving overall selectivity and sensitivity. For example, leveraging the physicochemical properties of PFOS as an anionic surfactant, researchers developed a detection method based on bubble nucleation mechanisms [10]. The core principle lies in the ability of PFOS molecules to significantly reduce the surface tension at the gas-liquid interface, thereby altering the nucleation energy barrier and kinetic behavior of gas bubbles (e.g., hydrogen or oxygen) during electrochemical processes. In cathodic hydrogen evolution reactions or anodic oxygen evolution reactions, the presence of PFOS modulates the nucleation overpotential and current response. By monitoring such surfactant-induced changes in bubble nucleation using cyclic voltammetry or chronoamperometry, quantitative analysis of PFOS concentrations can be achieved with an initial limit of detection (LOD) of 60 ppb.

1.2.2 Fluorescent Sensing Technology for PFOS

Fluorescence sensing is also a sensitive detection technique. It relies on specific interactions between fluorescent materials and target analytes to induce changes in fluorescence intensity, thereby enabling quantitative detection. Owing to its simple operation, strong practicality, and high signal sensitivity, fluorescence sensing has been developed rapidly in analytical detection. Researchers have designed a variety of fluorescence sensing strategies and employed different types of fluorescent materials as signal-responsive probes. It should be noted that PFOS lacks intrinsic fluorescence and cannot be detected directly via fluorescence signals. However, fluorescent probes can modulate their fluorescence intensity through specific interactions with PFOS, providing a feasible pathway for the fluorescence-based detection of PFOS [15]. Fluorescent sensors are typically classified into two types, which are turn-on (signal enhancement) and turn-off (signal quenching) types. Turn-on sensing generally relies

2026 S. T. Yau High School Science Award
仅用于2026丘成桐中学科学奖论文公示

on the restoration of fluorescence. A fluorescent probe is pre-quenched by a quencher, and the target analyte competitively binds the quencher, releasing the probe and recovering its fluorescence. For instance, Tan's group developed three competitive turn-on systems using carbon dots, eosin Y, or erythrosin B as probes paired with different quenchers, achieving detection of PFOS [16]. Another turn-on strategy involves directly synthesizing functionalized probes whose fluorescence changes upon target binding, such as molecularly imprinted polymer-carbon quantum dot composites applied to PFOS detection in serum and urine [17]. On the other hand, turn-off sensing is based on fluorescence decrease caused by probe-analyte interactions, which can occur via static quenching (non-fluorescent complex formation) or dynamic quenching (collisional deactivation). Various turn-off sensors have been reported, including cationic porphyrins [18], carbon quantum dots [19], and upconversion nanoparticle-covalent organic framework probes [20]. The latter demonstrated a detection limit as low as 0.15 pM for PFOS and was confirmed to operate predominantly through dynamic quenching.

1.2.3 Point of Care Testing Sensor

Nevertheless, both conventional instrumental methods and existing rapid detection approaches for PFOS are largely limited to laboratory use, failing to meet the growing demand for on-site rapid analysis. Point of care testing (POCT), also referred as on-site rapid detection, enables immediate sample pretreatment and analysis at the sampling site. Characterized by the portability, rapid-detecting speed and low cost, POCT eliminates the need for specialized laboratories, well-trained technicians and costly instruments, making it suitable for broad applications including clinical emergency diagnosis, food safety monitoring, and environmental surveillance [21-23].

Benefiting from rapid testing, simple operation and visible signal readouts, lateral flow assay (LFA) has become one of the most popular POCT technologies for practical applications. As a typical POCT technology that relies on specific binding between recognition elements and targets, LFA features a compact structural design composed of five key components, namely a sample pad, a conjugate pad, a reaction pad, an absorbent pad, and a backing card [24]. The sample pad is used to load crude samples

2026 S.T. Yau High School Science Award
仅用于2026丘成桐中学科学奖论文公示

such as blood and urine (Fig. 1.2). Its hydrophilic modification helps accelerate sample diffusion and remove impurities, thereby mitigating matrix interference in subsequent reactions. The conjugate pad is pre-coated with labeled recognition reagents, where colloidal gold, fluorescent microspheres, quantum dots, and latex particles serve as commonly used signal labels. The reaction pad, generally a nitrocellulose (NC) membrane, forms the core of the LFA strip. Two capture lines are immobilized on this membrane. The test line (T line) is coated with capture reagents (e.g., antigens or antibodies) for the target analytes, while the control line (C line) is coated with secondary antibodies that specifically binds the labeled probes from the conjugate pad, thus verifying the validity of the entire detection process. The absorbent pad, made of superabsorbent materials, generates capillary force to drive the lateral flow of the sample and labeled conjugates, absorbs excess solution after the reaction, and maintains stable operation of the chromatographic system.

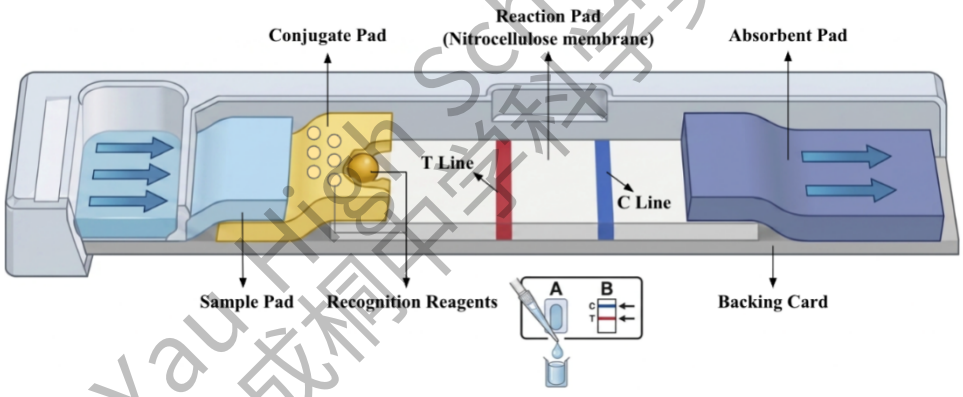


Figure 1.2. Typical structure of lateral flow assay (LFA).

The commercial pregnancy test strip (PTS), the most mature and widely used POCT product for home use, is a successful example of a lateral flow assay device. Its core mechanism relies on capillary action to drive urinary human chorionic gonadotropin (hCG) to bind with colloidal gold labeled anti-hCG antibodies preloaded on the conjugate pad, forming immune complexes. These complexes are subsequently captured by anti-hCG antibodies immobilized on the T line of the reaction membrane, generating a visible red color signal for rapid visual diagnosis. This design enables rapid detection at an extremely low cost (1 RMB) with negligible background interference, as hCG is normally produced only during pregnancy [25].

2026 S.T. Yau High School Science Award
仅用于2026丘成桐中学科学奖论文公示

After decades of development, PTS has evolved from a laboratory-exclusive testing technique into a prevalent portable household diagnostic product, with continuous performance upgrades in detection sensitivity, portability and user operability. Establishing a correlation between hCG concentration and the non-hCG target concentration is the key to integrating sensing strategies with PTS. In 2017, Du et al. first reported a signal transduction strategy that combined loop-mediated isothermal amplification (LAMP), DNA toehold-mediated strand displacement, and an hCG-DNA conjugate probe for the detection of nucleic acid biomarkers, such as Ebola virus and melanoma-related single-nucleotide polymorphisms [26]. In this approach, the nucleic acid biomarker induces LAMP to generate large DNA products that capture the hCG-DNA conjugate probe (Fig. 1.3a). The captured probe is prevented from migrating on the PTS, thereby converting the biomarker concentration into a measurable hCG signal. Subsequently, researchers developed a series of PTS-based sensing strategies, extending the detectable targets from single-stranded DNA biomarkers [27-29] to double-stranded DNA [30] and even non-nucleic acid targets [30–34]. For non-nucleic acid targets, current mainstream integration strategies can be divided into two types. The first one is fluidic blocking, and the second is enzyme-assisted release of hCG-DNA complexes. In the former strategy, the ssDNA-hCG conjugate probe is immobilized on large substrates such as magnetic beads [35,36], graphene [37,38], iron oxide [39], or DNA nanostructures [30], which hinders its migration on the PTS. Subsequent strand displacement or competitive binding then releases the probe, allowing it to migrate and produce a colorimetric signal. In contrast, the enzyme-assisted strategy employs CRISPR/Cas cleavage to release hCG from the hCG-DNA complex (Fig. 1.3b), after which the hCG in the supernatant is detected by a PTS to determine the target concentration [30,40,41].

2026 S.-T. Yau High School Science Award
仅用于2026丘成桐中学科学奖论文公示

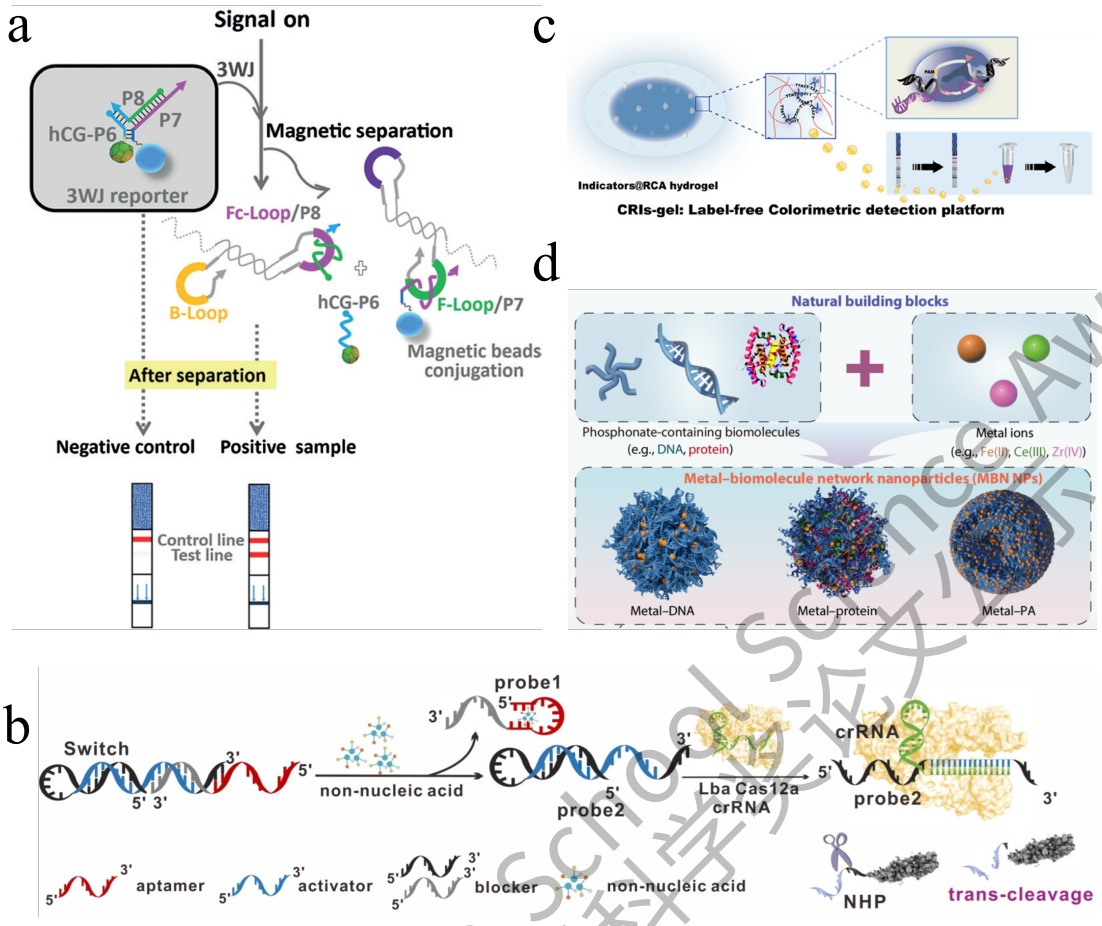


Figure 1.3. (a, b) Commercial pregnancy test strip using an hCG-DNA conjugate probe for the detection of (a) nucleic acid [26] and (b) non-nucleic acid targets [30]. (c) Commercial pregnancy test strip using a DNA hydrogel for nucleic acid detection [42]. (d) Interaction of metal ions with phosphonate-containing biomolecules (e.g., proteins and DNA) [43].

In these sensing strategies, hCG is typically immobilized through covalent conjugation to DNA, forming an ssDNA-hCG conjugate probe as an intermediate. However, these hCG-DNA conjugate-based signal conversion strategies suffer from the complex covalent conjugation between ssDNA and hCG, which may mask the active sites of hCG and thereby reduce detection efficiency. Non-conjugation signal transduction strategies have been shown to enhance the versatility and operational practicality of POCT. For example, Liu et al. encapsulated hCG in a DNA hydrogel prepared by rolling circle amplification (Fig. 1.3c), and then released hCG by cleaving the hydrogel using the trans cleavage activity of CRISPR/Cas12a [42]. However, since hCG is tightly wrapped by the DNA strands, the required cleavage time is as long as 5

2026 S.-T. Yau High School Science Award
仅用于2026丘成桐中学科学奖公示

hours, which contradicts the rapid detection principle of POCT. Therefore, there is an urgent need to develop non-conjugation signal transduction strategies with rapid response characteristics to facilitate the application of PTS in non-nucleic acid targets.

Both proteins and DNA can interact with metal ions via coordination or electrostatic interactions (Fig. 1.3d), leading to the modulation of their biological recognition performance [43,44]. This unique characteristic enables metal ions to act as temporary inhibitors for blocking specific protein-antibody recognition. Subsequent displacement of metal ions by competitive DNA molecules precisely switches the recognition state and regulates the corresponding sensing signal. Aptamers are single-stranded nucleic acid recognition ligands screened in vitro through the systematic evolution of ligands by exponential enrichment (SELEX). Benefiting from high affinity, excellent specificity, favorable stability, facile synthesis and modification, broad target versatility, and low cost, aptamers have emerged as ideal recognition elements for the construction of high-performance POCT biosensors [45]. To date, PFOS-targeting aptamers have been successfully screened and reported [46]. The integration of aptamer-based target recognition and metal ion-mediated modulation of hCG immunoactivity provides a feasible and innovative strategy for the signal transduction of PFOS detection.

1.3 Objectives and Innovations

This study intends to develop a microfluidic chip-based PTS biosensor that integrates aptamer-based recognition probes (Fe_3O_4@Au@cDNA@Apt) with Zr^{4+}-mediated modulation of hCG immunoactivity for PFOS detection. As shown in Fig. 1.4, the sample containing the recognition probe and PFOS is introduced through one inlet. Upon PFOS binding, the aptamer dissociates from the probe. After magnetic separation, the supernatant containing the released aptamer is mixed with Zr^{4+} (introduced from a second inlet) to form Zr^{4+}-aptamer chelates. These chelates prevent Zr^{4+} from inhibiting the immunoactivity of subsequently added hCG, thereby allowing normal T line recognition and producing a positive signal. In the absence of PFOS, free Zr^{4+} binds directly to hCG, blocking antibody recognition and yielding a negative signal. The resulting color change on the T line enables rapid visual detection. Finally, the T line signal can be captured by a smartphone and analyzed with ImageJ software for

2026 Sir Yau High school Science Award
仅用于2026丘成桐中学科学奖论文公示

quantitative PFOS detection.

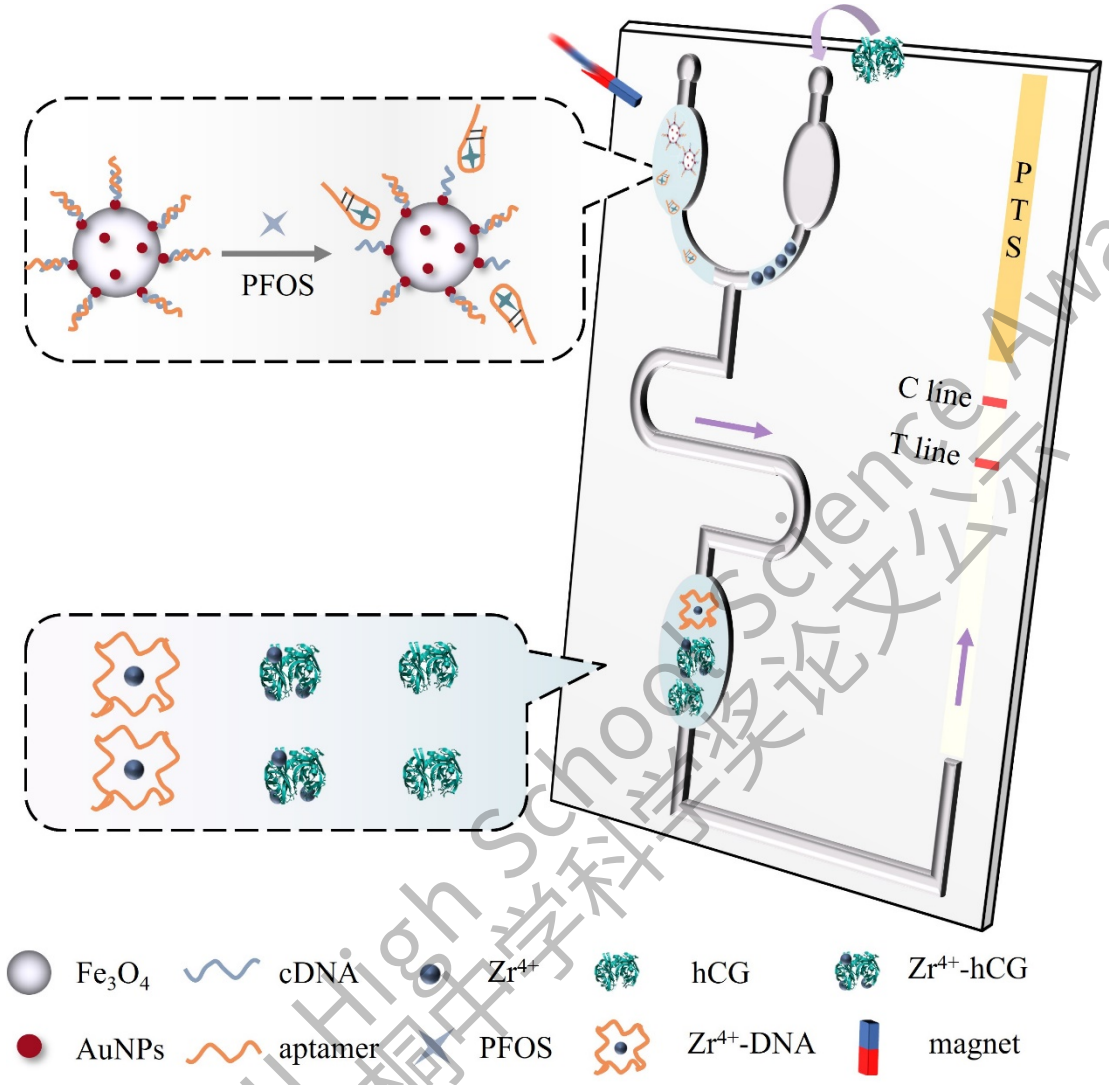


Figure 1.4. Schematic illustration of the microfluidic chip-based PTS biosensor employing Fe_3O_4@Au@cDNA@Apt recognition probes and Zr^{4+}-mediated modulation of hCG immunoactivity for signal transduction.

2. Methods

2.1 Chemicals and Materials

The Perfluorooctanesulfonic acid potassium (PFOS-K) was purchased from Alta (Shanghai, China). Perfluorooctanoic acid (PFOA), perfluorohexanoic acid (PFHxA), perfluoropentanoic acid (PFPeA), perfluorononanoic acid (PFNA), perfluoro-1-butanesulfonic acid (PFBS), trisodium citrate dihydrate and 6-mercapto-1-hexanol (MCH) were ordered from Macklin (Shanghai, China). 4-(2-Hydroxyethyl) piperazine-1-ethanesulfonic acid (HEPES), sodium chloride (NaCl), magnesium chloride

2026 S.-T. Yau High School Science Award
仅用于2026丘成桐中学科学奖论文公开

hexahydrate ($MgCl_2 \cdot 6H_2O$), sodium acetate (CH_3COONa), ethylene glycol (EG) and carboxymethyl cellulose (CMC) were purchased from Aladdin Industrial Inc. (Shanghai, China). Iron (III) chloride ($FeCl_3$) and zirconium (IV) chloride ($ZrCl_4$) were purchased from Energy Chemical (Shanghai, China). Hydrogen tetrachloroaurate (III) trihydrate ($HAuCl_4 \cdot 3H_2O$) and ethanol (C_2H_5OH) were purchased from Sinopharm (Beijing, China). Human chorionic gonadotropin (hCG) was ordered from Biosynth (Lake constance, Switzerland).

All the DNA oligonucleotides (Table 2.1) were synthesized and purified by Saigon Biotech (Shanghai, China). All the oligonucleotides had one thiol (SH) label at the 5' terminal with a TEG (tetraethyleneglycol) linker. Binding buffer for PFOS detection contained 10 mM HEPES (pH 7.0), 10 mM $MgCl_2$, 200 mM NaCl and 10 mM KCl. Ultrapure water used in this experiment was obtained by a Purelab Ultra Genetic Elga Labwater system (UK). Other reagents used in the experiment were of analytical grade.

Table 2.1. List of oligonucleotide sequences

Name	Sequences (5' to 3')
Apt	CTCTCGGGACGACGGGGTAACGGTTTGATCTCCTTCGTG TTCTGTCGTCCC
C1	TTTTTTAACCGTTACCCC
C2	TTTTTTACCGTTACCCCG
C3	TTTTTTCCGTTACCCCGT
C4	TTTTTTCGTTACCCCGTC
SH-labeled C2	SH- TTTTTTACCGTTACCCCG
SH-Apt	SH- CTCTCGGGACGACGGGGTAACGGTTTGATCTCCTTCGTG TTCTGTCGTCCC

2.2 Apparatus

X-ray diffraction (XRD) patterns were recorded on an X'Pert PRO diffractometer (PANalytical, Netherlands). Morphologies were characterized using a RE-2000A scanning electron microscope (SEM, Hitachi, Japan) and a Tecnai G2 transmission electron microscope (TEM, FEI, USA). UV-vis absorption spectra were collected on an Agilent-8453 spectrophotometer (Agilent Technologies, USA). Circular dichroism (CD) spectra were obtained using a J-1500 spectropolarimeter (JASCO, Japan). Zeta potential measurements were performed on a ZEN-3700 analyzer (Malvern Panalytical,

2026 S.T. Yau High School Science Award
仅用于2026丘成桐中学科学奖论文公示

UK). Magnetic properties were characterized using an 8604 vibrating sample magnetometer (VSM, Lake Shore, USA). Polyacrylamide gel electrophoresis (PAGE) was performed on a Mini-Sub Cell GT system (Bio-Rad, USA). A CP100NX ultracentrifuge (Hitachi, Japan), a DZF-6053 vacuum drying oven (Yiheng, Shanghai, China) and a DF-101S magnetic heating stirrer (Yuhua, Gongyi, China) were used for sample preparation.

2.3 Sequence Optimization and Affinity Evaluation of the PFOS-Specific Aptamer and Its Complementary DNA

The PFOS-specific aptamer was derived from a previous report [46], followed by the design and sequence length optimizations of its complementary DNA (cDNA). The binding affinity between the aptamer and PFOS was evaluated by PAGE. Prior to use, aptamer and cDNA (10 μM) were annealed by heating to 95 °C for 5 min, followed by cooling down to room temperature. PAGE (12%) was performed in 1 × TBE buffer (90 mM Tris-base, 90 mM boric acid, 2 mM EDTA, pH 8.3). For binding assays, the aptamer (1 μM), cDNA (1 μM), and PFOS (5 μM) were incubated in HEPES buffer for 60 min. Then, 10 μL of sample was mixed with 2 μL of 6 × loading buffer and 2 μL of SYBR Gold. The mixture solution was loaded into the corresponding wells, and electrophoresis was run at 110 V for 60 min. Finally, the gel was imaged using a Bio-Rad imaging system.

2.4 Fabrication of the Fe_3O_4@Au@cDNA@Apt Magnetic Recognition Probes and Fe_3O_4@Au@Apt Magnetic Enrichment Probes

Citrate-modified Fe_3O_4 nanospheres were prepared via hydrothermal method in the presence of sodium citrate [47]. Fe_3O_4@Au nanospheres were then synthetized according to a previously reported procedure [48], in which the citrate-coated Fe_3O_4 nanospheres served as seeds for the nucleation and growth of gold nanoparticles (AuNPs) on the Fe_3O_4 surface through the reduction of $HAuCl_4$ by sodium citrate (Fig. 2.1a).

The recognition probe (Fe_3O_4@Au@cDNA@Apt) was carried out via a two-step procedure involving cDNA immobilization followed by aptamer hybridization. Fe_3O_4@Au@cDNA nanoparticles were prepared via the formation of Au-S bonds

2026 S. T. Yau High School Science Award 仅用于2026丘成桐中学科学奖论文公示

between activated SH-labeled cDNA and Fe_3O_4@Au nanoparticles. Briefly, 1 mL of the as-prepared Fe_3O_4@Au nanospheres suspension (5 mg·mL^{-1}) was mixed with 10 μL of activated cDNA solution (final concentration, 2 μM) and incubated on a rotator for 18 h at room temperature (Red samples, Fig. 2.1b). The nanoparticles were then magnetically washed three times with 10 mM HEPES buffer. Subsequently, the product was dispersed in 1 mL of 10 μM 6-mercapto-1-hexanol (MCH) solution and incubated on a rotator for 1.5 h at room temperature to block the remaining gold surface and prevent nonspecific adsorption. The MCH-blocked nanoparticles were magnetically washed three times with 10 mM HEPES buffer and re-dispersed in 1 mL of the same buffer. The aptamer solution (final concentration, 4 μM) was then added to the above Fe_3O_4@Au@cDNA material, and incubated on a rotator for 1 h at room temperature. After another three rounds of magnetic washing with 10 mM HEPES buffer, the final functionalized Fe_3O_4@Au@cDNA@Apt nanoparticles (5 mg·mL^{-1}) were stored at 4 °C. The enrichment probes for PFOS were prepared following the same procedure as described for Fe_3O_4@Au@cDNA, except that the SH-labeled aptamer was used instead of cDNA, at a final concentration of 2 μM (Blue samples Fig. 2.1b).

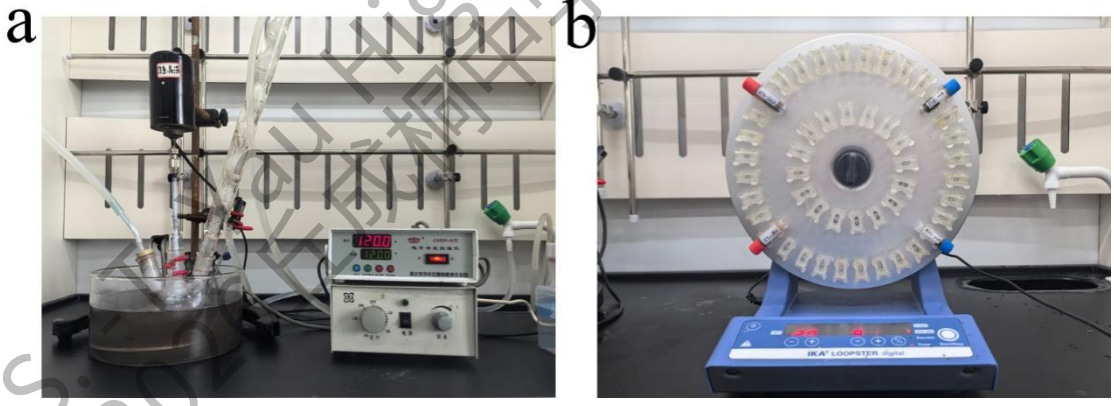


Figure 2.1. Reaction equipment for the fabrication of Fe_3O_4@Au nanospheres (a) and Fe_3O_4@Au@cDNA@Apt recognition probes and Fe_3O_4@Au@Apt enrichment probes (b).

2.5 Quantitative Detection of PFOS

For PFOS quantification, a 50 μL reaction mixture was prepared containing 30 μL of the Fe_3O_4@Au@cDNA@Apt recognition probe (5 mg·mL^{-1}), 10 μL of binding buffer (10 mM HEPES (pH 7.0), 10 mM $MgCl_2$, 200 mM NaCl, 10 mM KCl), and 10 μL of various concentrations of PFOS standard solution (final concentration, 10-400 μM).

2026 Shanghai High School Science Award
仅用于2026上海市高中科学奖论文公示

The mixture was incubated at room temperature for 40 min. After magnetic separation, 40 μL of the supernatant was collected and sequentially incubated with 5 μL of Zr^{4+} (200 μM) for 10 min and then with 5 μL of hCG (5 μg·mL^{-1}) for 20 min. A PTS was then inserted into the solution (Fig. 2.2a). After 5 min, the color intensity of the T line was captured with a smartphone and analyzed using ImageJ software (Fig. 2.2b). A standard curve was constructed with PFOS concentration and T line intensity as the x-axis and the y-axis.

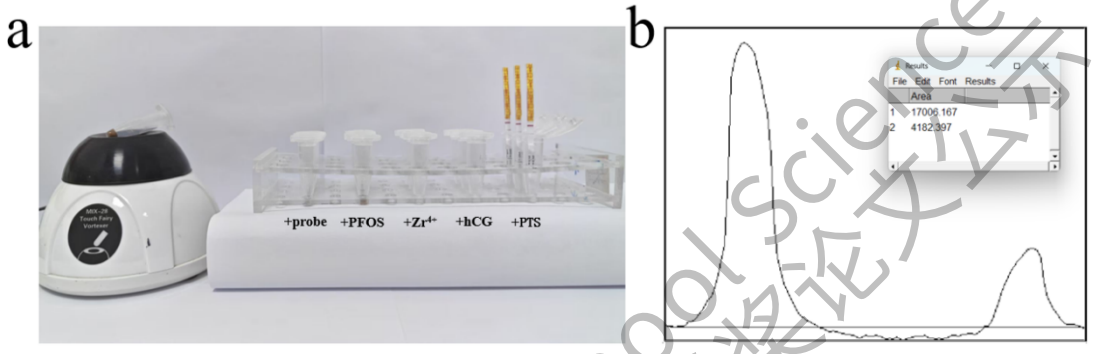


Figure 2.2. Operation procedure (a) and signal analysis software (b) for the detection of PFOS.

2.6 Investigation of Signal Transduction Mechanism Based on hCG Immunoactivity Regulation

Circular dichroism (CD) spectroscopy was employed to examine the conformational changes of hCG upon interaction with Zr^{4+} and a Zr^{4+}/DNA mixture. CD spectra were recorded on a J-1500 spectropolarimeter at 25 °C using a quartz cuvette with a 1 mm path length. The scanning wavelength ranged from 190 to 400 nm, with a scan rate of 100 nm min^{-1} and a sampling interval of 0.2 nm. Measurements were carried out on hCG solution (200 μg·mL^{-1}, 0.5 mL), a Zr^{4+}/hCG mixture (200 μg·mL^{-1} hCG with 5 mM Zr^{4+}) and a DNA/Zr^{4+}/hCG mixture prepared by incubating 2 μM DNA with 5 mM Zr^{4+} prior to the addition of 200 μg·mL^{-1} hCG. The secondary structure content of hCG was calculated from the CD data using CDNN software.

In parallel, UV-vis absorption spectroscopy was used to monitor the conformational changes of hCG under identical interaction conditions, based on the absorbance at 200 nm. Measurements were carried out on hCG solution (20 μg·mL^{-1}), a Zr^{4+}/hCG mixture (20 μg·mL^{-1} hCG with 4 mM Zr^{4+}) and a DNA/Zr^{4+}/hCG mixture obtained by first incubating 2 μM DNA with 4 mM Zr^{4+} and subsequently adding 20 μg·mL^{-1} hCG.

2026 S.T. Yau High School Science Award
仅用于2026丘成桐中学科学奖论文公示

Absorption spectra were recorded in the range of 190-330 nm with a sampling interval of 0.2 nm.

2.7 Magnetic Enrichment of PFOS

For the spiking experiment, PFOS standard solution was added to a real environmental water sample to a final concentration of 200 nM. The resulting solution (total volume, 40 mL) was then incubated with Fe_3O_4@Au@Apt magnetic enrichment probes under shaking at room temperature for 15 min. After magnetic separation, the supernatant was discarded, and the PFOS-loaded enrichment probes were transferred into 40 μL of ultrapure water, yielding a 1000-fold enrichment. The probes were then heated in a 70 °C water bath with shaking for 6 min to fully desorb PFOS. This adsorption-desorption cycle was repeated three times to complete the enrichment. The enrichment factor was adjusted by changing the final desorption volume. Real environmental samples were processed following the same procedure as described above, except that the enrichment probes were added directly to the pretreated samples without spiking.

2.8 Development of the Microfluidic Chip

The microfluidic chip (Nanjing Lishi Micro-Nano Technology Co., Ltd., Nanjing, China) was equipped with three parallel serpentine channels, which were equipped with negative control, PFOS sample, and positive control for guaranteeing the practicability. To adapt the chip for our assay, the inlet, fluidic channels, reaction chamber and PTS detection zone were integrated on this chip. The design of the microfluidic chip is illustrated in Fig. 2.3. The double-layer PMMA microfluidic chip (80 mm × 100 mm) contains three parallel serpentine channels. The three channels were designed for negative control, PFOS sample, and positive control, respectively. Each channel integrates a sample inlet, a reaction chamber, and a PTS detection zone. The channel layer (3 mm) and cover layer (2 mm) were bonded by plasma-activated thermal compression (Fig. 2.3a-c). The finished chip exhibits clear channel edges (Fig. 2.3d), providing a stable platform for magnetic enrichment and PTS readout.

2026 S. T. Yau High School Science Award
仅用于2026丘成桐中学科学奖论文公示

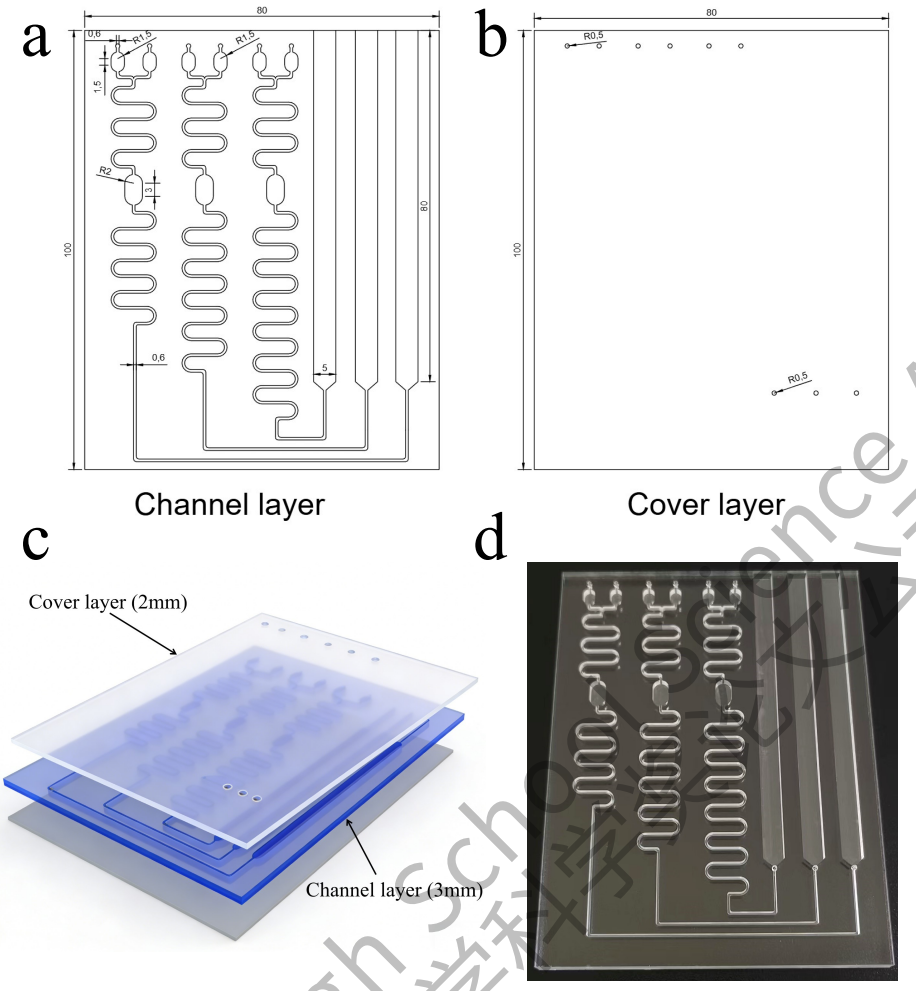


Figure 2.3. Design and assembly of the microfluidic chip. (a) Channel layer, (b) Cover layer, (c) Schematic diagram of the assembled chip, and (d) Photograph of the device.

To assess the sealing performance and fluidic behavior of the fabricated microfluidic chip, rhodamine B and fluorescein sodium solutions were used as fluorescent tracers. The flow characteristics and channel integrity were visually examined under fluorescence microscopy.

2.9 Collection and Pretreatment of Environmental Water Samples

To evaluate the practical applicability of the developed integrated microfluidic chip-PTS sensor, representative environmental water samples were collected from multiple locations. Surface water samples were obtained from the Lanzhou, Zhengzhou, and Jinan sections (covering upper, middle, and lower reaches) of the Yellow River. After collection, the water samples were immediately filtered through 0.22 μm membrane filters to remove suspended particles and microorganisms. The obtained samples were stored in refrigerator (4 °C) for further use.

2026 S. T. Yau High School Science Award
仅用于2026丘成桐中学科学奖公示

2.10 Integrated Detection of Environmental Pollutants Using Magnetic Enrichment Coupled with the Microfluidic Chip

Magnetic enrichment of PFOS from the pretreated surface water samples was performed according to the procedure described in Section 2.7. After enrichment, the obtained desorption solution (40 μL) was used to dissolve the water-removed Fe_3O_4@Au@cDNA@Apt (30 μL), followed by the addition of 10 μL of binding buffer. The mixture was then magnetically separated, and the supernatant was collected.

The supernatant was mixed with Zr^{4+} to a final concentration of 20 μM, and 40 μL of the mixture was introduced into inlet 1 of the microfluidic chip. After 10 min, 5 μL of human chorionic gonadotropin (hCG) solution (5 $\mu g \cdot mL^{-1}$) was added into another inlet. The liquids were then driven into the reaction chamber for further 20 min of incubation. Following the reaction, the mixture was pushed toward the chip outlet, where capillary action drove the liquid flow along the PTS for signal readout and quantitative detection. The desorption solution was replaced by the binding buffer and PFOS standard solution for negative control and positive control channel, respectively.

3. Results and Discussion

3.1. Characterization of Fe_3O_4@Au@cDNA@Apt Magnetic Recognition Probes

The preparation of Fe_3O_4@Au nanoparticles was investigated by scanning electron microscopy (SEM) and transmission electron microscopy (TEM). Fe_3O_4 possesses a spherical structure (Fig. 3.1a and 3.1b) with an average diameter of 310 nm (Fig. 3.1c). After in-situ plating gold, a large amount of AuNPs was observed on the Fe_3O_4 surface (Fig. 3.1d and 3.1e). The average diameter of Fe_3O_4@Au nanospheres was about 330 nm, a slight increase from that of Fe_3O_4 (Fig. 3.1c) attributable to the Au decoration (Fig. 3.1f).

2026 S.-T. Yau High School Science Award
仅用于2026丘成桐中学科学奖论文公示

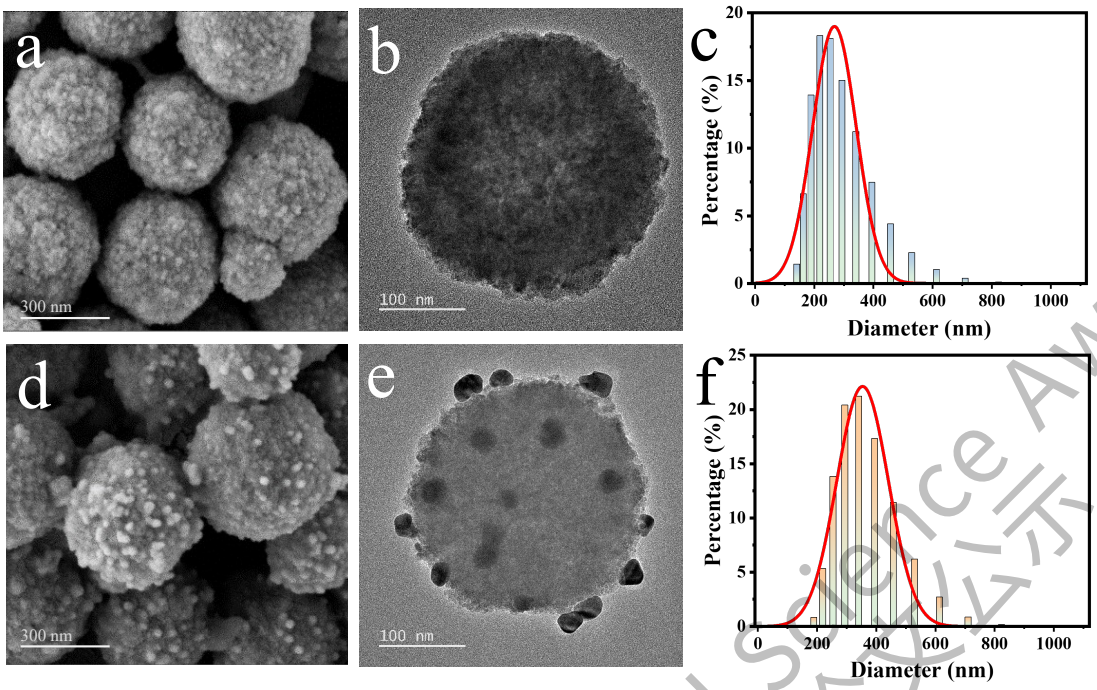


Figure 3.1. SEM (a) and TEM (b) images of Fe_3O_4, (c) particle size distribution of Fe_3O_4, SEM (d) and TEM (e) images of Fe_3O_4@Au, and (f) particle size distribution of Fe_3O_4@Au.

The X-ray diffraction (XRD) patterns of Fe_3O_4@Au exhibited characteristic peaks at $2\theta = 30.3°$, 35.7°, 43.3°, 54.1°, 57.4°, and 62.9° (Fig. 3.2a), corresponding to the (220), (311), (400), (422), (511), and (440) planes of Fe_3O_4 [49]. Moreover, additional peaks (blue symbols) at 38.2°, 44.5°, 64.5°, and 77.5° matched the characteristic peaks of Au [50], further confirming the successful synthesis of Fe_3O_4@Au nanoparticles.

Before the fabrication of Fe_3O_4@Au@cDNA@Apt probes, the cDNA for PFOS-specific aptamer needed to be identified. Previous studies have demonstrated that, the selected Apt exhibits the highest binding affinity toward PFOS among reported nucleic acid sequences [46]. To realize the competing reaction between cDNA with PFOS, a series of cDNAs with different lengths were designed to determine the most suitable cDNA for subsequent experiments. As shown in Fig. 3.2b, C2 formed a stable duplex with the Apt and allowed efficient displacement by PFOS (lanes 4-5). In contrast, C1 hybridized weakly (lanes 2-3), while C3 and C4 induced only minor band shifts upon PFOS addition (lanes 6-7 and lanes 8-9). Therefore, the Apt/C2 pair was selected as the optimal recognition pair.

2026 S.-T. Yau High School Science Award
仅用于2026丘成桐中学科学奖公示

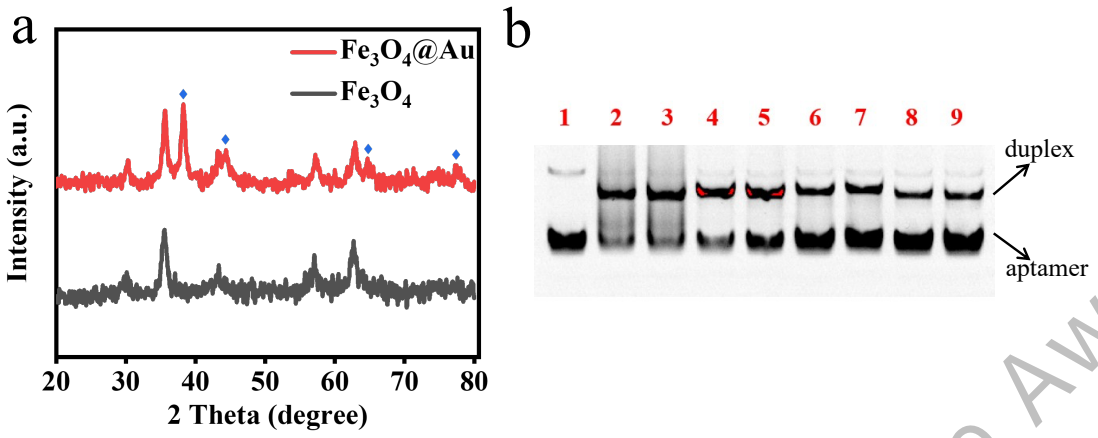


Figure 3.2. (a) XRD patterns of Fe_3O_4 and Fe_3O_4@Au; (b) PAGE analysis of the effect of cDNA length on aptamer binding to PFOS. Lanes 1, 2, and 3 show Apt alone, Apt + C1, and Apt + C1 + PFOS, respectively. Lanes 4 and 5 show Apt + C2, and Apt + C2 + PFOS, respectively. Lanes 6 and 7 show Apt + C3, and Apt + C3 + PFOS, respectively. Lanes 8 and 9 show Apt + C4, and Apt + C4 + PFOS, respectively.

Then, the selected APT/C2 pair was immobilized onto Fe_3O_4@Au nanoparticles to construct Fe_3O_4@Au@cDNA@Apt recognition probe, in which the cDNA strand (C2) was first conjugated to the Fe_3O_4@Au surface and the aptamer was subsequently hybridized to the cDNA. After duplex modification, the probe exhibited a more negative zeta potential (-35 mV) than Fe_3O_4@Au (-26 mV) (Fig. 3.3a), attributed to the negatively charged phosphate backbone of DNA. Moreover, UV-vis spectroscopy of Fe_3O_4@Au@cDNA@Apt probe showed a characteristic DNA absorption peak at 260 nm (Fig. 3.3b), further confirming the successful loading of the cDNA/Aptamer duplex [51]. The superparamagnetism of Fe_3O_4@Au@cDNA@Apt probe was also investigated for assuring the rapid separation in the experimental workflow. As shown in Fig. 3.3c, all three samples (Fe_3O_4, Fe_3O_4@Au, and Fe_3O_4@Au@cDNA@Apt) exhibited superparamagnetic behavior with no hysteresis. The saturation magnetization (Ms) of the probe (60.31 emu·g^{-1}) was similar to that of Fe_3O_4@Au (60.34 emu·g^{-1}) but notably lower than that of uncoated Fe_3O_4 (74.69 emu·g^{-1}). The decrease in saturation magnetization of 9.75 emu·g^{-1} after Au deposition was attributed to the non-magnetic Au shell. Subsequent DNA functionalization caused only a negligible further reduction, indicating that the magnetic core remained intact. Moreover, as demonstrated in the

2026 S.-T. Yau High School Science Award
仅用于2026丘成桐中学科学奖论文公示

inset of Fig. 3.3c, the probe could be fully captured by an external magnet within 5 s, demonstrating its excellent magnetic responsiveness and suitability for the multiple separation steps required in subsequent experiments.

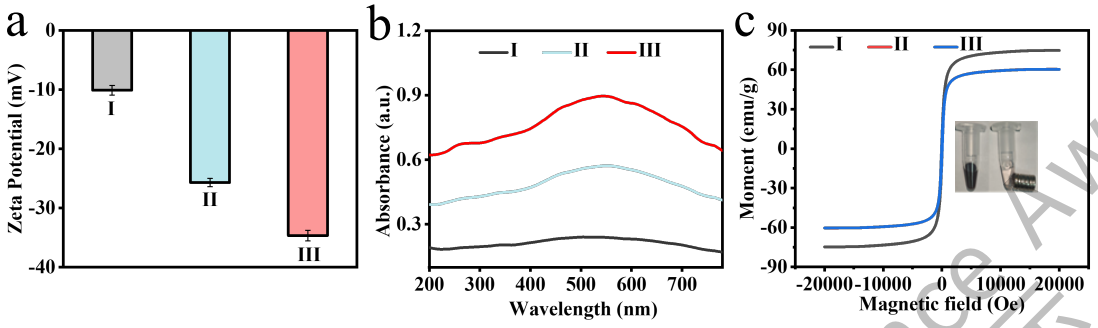


Figure 3.3. (a) Zeta potentials, (b) UV-vis absorption spectra and (c) magnetization curves of different samples. I represents Fe_3O_4, II represents Fe_3O_4@Au, III represents Fe_3O_4@Au@cDNA@Apt. Inset in (c) shows a photograph of magnetic separation.

3.2. Feasibility of the Sensing Strategy and Mechanism of Zr^{4+}-Regulated hCG Immunoactivity

The proposed signal transduction mechanism was first examined by PTS. As shown in Fig. 3.4a, upon addition of Zr^{4+} (20 μM) to hCG (0.2 μg·mL^{-1}), the T line signal decreased sharply from 5506 to 1435. However, when the Zr^{4+}/DNA mixture was introduced into the hCG solution, the signal was as high as 5243. Control experiments confirmed that neither DNA nor Zr^{4+} alone interfered with strip operation, as there were no signals at the T line yet the control (C) line remained visible in these cases. Furthermore, after pre-incubation of hCG with PFOS, the T line signal remained at 5321, indicating that PFOS had a negligible effect on the immunoactivity of hCG. These results together confirmed that DNA can competitively bind to Zr^{4+} and thereby protect hCG from inhibition.

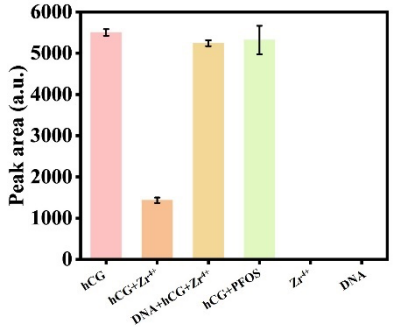


Figure 3.4. Effects of different components on the response of PTS.

2026 S.-T. Yau High School Science Award
仅用于2026丘成桐中学科学奖公示

To elucidate how Zr^{4+} modulates hCG immunoactivity, UV-vis absorption tests were performed. As shown in Fig. 3.5a, hCG exhibited a characteristic absorption peak at 205 nm, which could be attributed to π-π* transition of the peptide backbone C=O. Upon addition of Zr^{4+} to the hCG solution, the absorbance at 205 nm decreased, suggesting a loosening or partial disruption of the backbone structure of hCG. When the Zr^{4+}/DNA mixture was added to the hCG solution, the absorbance at 205 nm still approximated to the original level, and the spectral profile characteristic of native hCG was well preserved. This conformational restoration indicates that DNA competitively binds to Zr^{4+}, thereby inhibiting Zr^{4+}-induced disruption of hCG structure. Circular dichroism (CD) spectroscopy was further employed to assess the effect of Zr^{4+} on the secondary structure of hCG. As shown in Fig. 3.5b, native hCG exhibited negative peaks at 208 nm and 222 nm (α-helix) and a band around 214 nm (β-sheet). Quantitative analysis using CDNN software [52] revealed that native hCG contained 15.7% α-helix, 27.0% β-sheet, 18.3% β-turn, and 39.0% random coil (Table 3.1). Upon exposure to Zr^{4+}, the α-helix content decreased to 13.0%, while β-sheet increased to 29.1%. Meanwhile, β-turn and random coil remained basically unchanged (18.5% and 39.4%, respectively). These findings suggest that the binding of Zr^{4+} to hCG mainly induced a partial transition from α-helix to β-sheet conformation, while the overall folding state did not undergo drastic rearrangement [53]. Such conformational change is likely the structural basis for the suppressed immunoactivity of hCG. Moreover, when DNA/Zr^{4+} mixture was added to the hCG solution, the α-helix content partially recovered from 13.0% to 14.7% and the β-sheet content decreased correspondingly from 29.1 to 27.8%. These results confirm that DNA can prevent Zr^{4+}-induced conformational disruption of hCG by competitively binding to Zr^{4+}, providing the molecular-level evidence for the signal transduction mechanism.

2026 S. T. Yau High School Science Award
仅用于2026丘成桐中学科学奖论文公示

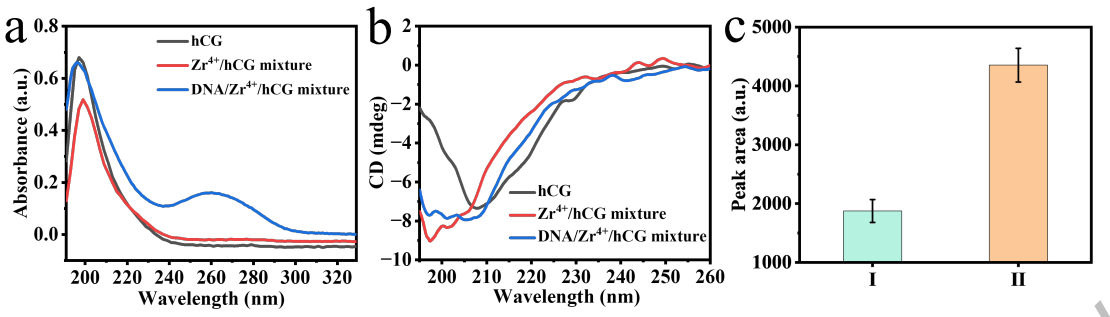


Fig. 3.5. (a) UV-vis absorption spectra of hCG, Zr^{4+}/hCG mixture and DNA/Zr^{4+}/hCG mixture. (b) CD spectra of hCG, Zr^{4+}/hCG mixture and DNA/Zr^{4+}/hCG mixture. (c) T line signals of the PTS sensor without PFOS (I) and with PFOS (II).

Table 3.1. Effect of Zr^{4+} and DNA/Zr^{4+} mixture on the percentage of secondary structural elements of hCG.

Component	α-helix	β-sheet	β-turn	unordered
hCG	15.7	27.0	18.3	39.0
Zr^{4+}+hCG	13.0	29.1	18.5	39.4
Zr^{4+}+DNA+hCG	14.7	27.8	18.5	39.0

Then, we further assessed the feasibility of Zr^{4+}-regulated hCG immunoactivity-based PTS sensor, with the recognition probe (Fe_3O_4@Au@cDNA@Apt) incubated in the absence and presence of PFOS. After magnetic separation, the supernatant was mixed with Zr^{4+} and hCG, and a PTS was inserted. The T line signal was captured by a smartphone and analyzed with ImageJ software. As shown in Fig. 3.5c, the introduction of PFOS caused an increase in the T line signal from 1874 to 4534. Such a result demonstrated that PFOS triggered the release of the aptamer from recognition probe, which subsequently bound Zr^{4+} and thereby blocked the Zr^{4+}-mediated inhibition of hCG.

3.3. Analytical Performance of the PTS Sensor for PFOS

As well known, the sensitivity of biosensor depends on the parameters of both the recognition and the signal transduction process. In the proposed PTS sensor, the amount of the recognition probe (Fe_3O_4@Au@cDNA@Apt) largely affects the recognition and signal transduction efficiency. Therefore, the dosage of the recognition probe was optimized. As shown in Fig. 3.6a, the T line signal intensity increased gradually with increasing probe amount. However, the signal intensity plateaued when the probe

2026 S.-T. Yau High School Science Award
仅用于2026丘成桐中学科学奖论文公示

amount reached 30 μL. Therefore, 30 μL was selected as the optimal amount for subsequent experiments. Also given the competitive recognition between PFOS-aptamer complex and the cDNA-aptamer duplex is time-dependent, the incubation time was then optimized. As shown in Fig. 3.6b, the T line signal intensity increased gradually with prolonged incubation, indicating that the binding of PFOS to the aptamer progressively approached saturation. The signal plateaued at 40 min, suggesting that the aptamer dissociation from the cDNA had reached a maximum and the system had attained equilibrium. Therefore, 40 min was determined as the optimal recognition time. Besides, the interaction time between Zr^{4+} and the aptamer is a critical factor affecting detection sensitivity. If hCG is introduced before the aptamer fully reacts with Zr^{4+}, residual Zr^{4+} may still inhibit the immunoactivity of hCG, thereby reducing the detection signal and limiting sensitivity. After aptamer dissociation from the Fe_3O_4@Au@cDNA@Apt recognition probe, the interaction times of Zr^{4+} with aptamer was systematically investigated. As shown in Fig. 3.6c, the T line signal intensity increased gradually with prolonged interaction time and plateaued at 8 min, indicating that the aptamer had reacted completely with Zr^{4+} and the immunoactivity of hCG was fully restored. Therefore, 8 min was selected as the optimal interaction time for Zr^{4+} and the aptamer. Finally, the interaction time between Zr^{4+} and hCG was optimized. As shown in Fig. 3.6d, the immunoactivity of hCG decreased progressively with longer incubation time and reached a minimum at 20 min, after which it remained stable, indicating that the inhibitory effect of Zr^{4+} on hCG had reached equilibrium. Therefore, 20 min was selected as the optimal interaction time for Zr^{4+} and hCG. Taken together, the optimal conditions were determined to be 30 μL of probe, 40 min probe-PFOS incubation, 8 min Zr^{4+}-DNA incubation, and 20 min Zr^{4+}-hCG incubation.

2026 Si-Yan High School Science Award
仅用于2026思源中学科学奖论文公示

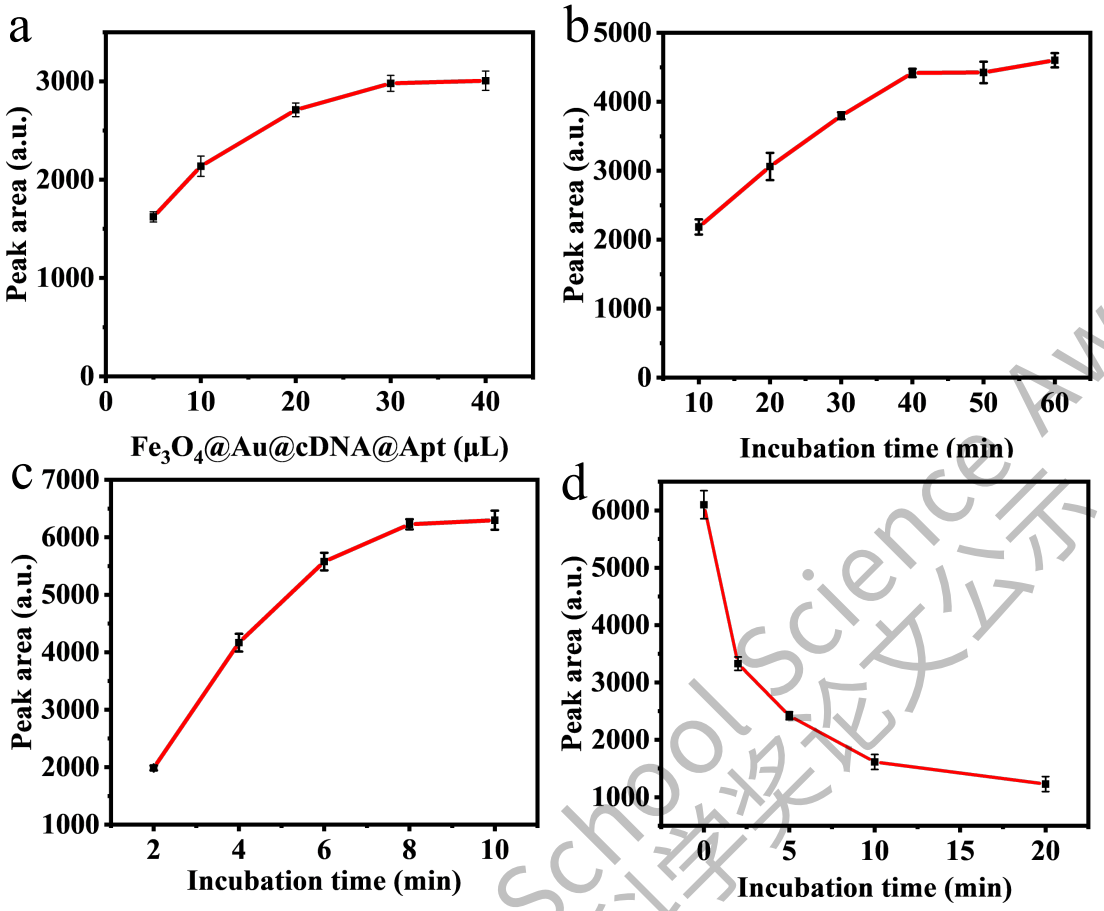


Figure 3.6. (a) Effect of the amount of the recognition probe on the T line signal. (b) Effect of the incubation time of PFOS with the recognition probe on the T line signal. (c) Effect of the interaction time between Zr^{4+} and DNA on the T line signal. (d) Effect of the interaction time between Zr^{4+} and hCG on the T line signal.

Under optimal conditions, the PTS sensor was applied to quantify PFOS. As shown in Fig. 3.7a, a visible T line signal appeared at a PFOS concentration of 10 μM (~5.0 ppm), and the signal intensity gradually enhanced with the increase of PFOS concentration. A good linear relationship was observed between the T line intensity and PFOS concentration over the range of 10-400 μM, and the linear equation is y = 2240.36 + 11.23 x (where y is the T line intensity and x is PFOS concentration in μM). The selectivity of the proposed PTS sensor was evaluated by using structurally similar perfluorinated compounds, including perfluorooctanoic acid (PFOA), perfluorobutanesulfonic acid (PFBS), perfluoropropionic acid (PFPA), perfluorohexanoic acid (PFHxA), and perfluorononanoic acid (PFNA). Each interferent was tested at a ten-fold higher concentration than PFOS. As shown in Fig. 3.7b, none

2026 S.-T. Yau High School Science Award 仅用于2026丘成桐中学科学奖论文公示

of these interferents produced a distinct T line signal, demonstrating that the T line signal is PFOS-specific. Such good specificity is attributed to the high recognition ability of the selected aptamer toward the molecular structure of PFOS.

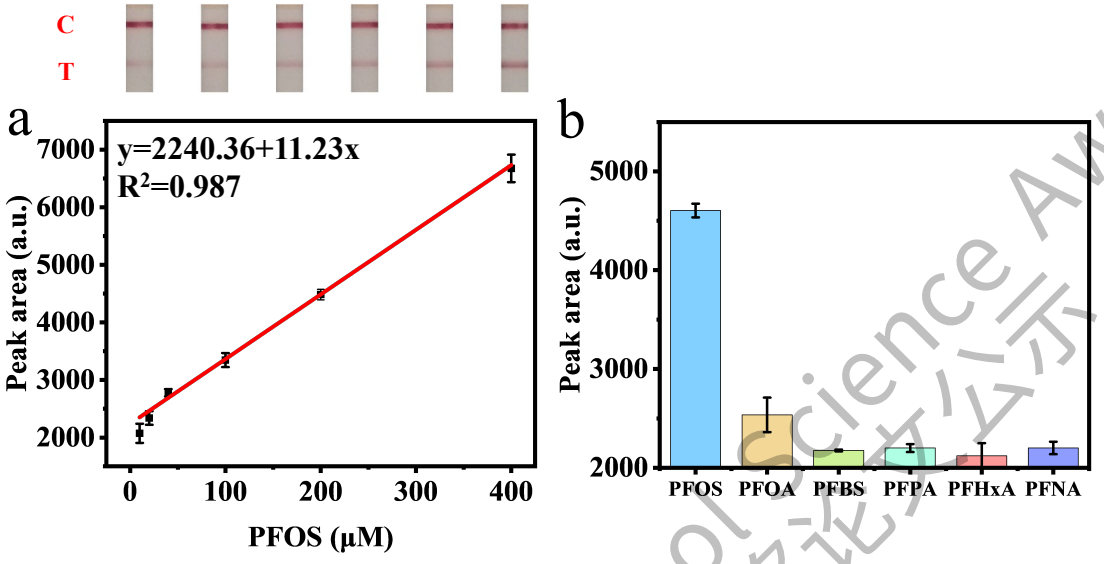


Figure 3.7. (a) The linear correlation between the T line signal and the PFOS concentration from 10-400 μM range. (b) Specificity investigation of PFOS against other analogues.

Nevertheless, the real environmental samples only contain low-abundance PFOS. Moreover, these real samples may also contain some metal ions, which can interfere with the detection. To enhance the sensitivity and anti-interference capability of the detection method, an aptamer-labeled magnetic enrichment probe (Fe_3O_4@Au@Apt) was constructed. The Fe_3O_4@Au@Apt probe was prepared following the same procedure as the Fe_3O_4@Au@cDNA of recognition probe, except that the cDNA was replaced with the PFOS aptamer. As shown in Fig. 3.8a, such magnetic enrichment probe can absorb the PFOS in the high-volume real samples due to the binding affinity between the aptamer and PFOS. Notably, the binding between aptamer and PFOS relies on non-covalent interactions, including hydrogen bonding, van der Waals forces, electrostatic interactions, and π-π stacking. Previous studies have demonstrated that elevated temperatures weaken these non-covalent interactions and disrupt the conformation required for binding, thereby inducing dissociation of the aptamer-target complex [36]. In this case, if the PFOS-absorbed Fe_3O_4@Au@Apt probes were dissolved into a low-volume solution, the highly-concentrated PFOS sample will be

2026 S.-T. Yau High School Science Award
仅用于2026丘成桐中学科学奖公示

obtained at high temperature (70 °C), due to desorption. Finally, the proposed PTS sensor can analyze these highly-concentrated sample for the realization of signal amplification.

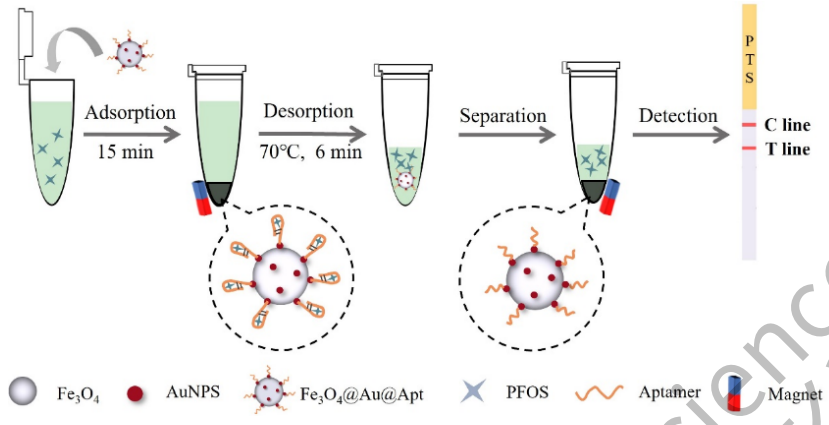


Figure 3.8. The adsorption-desorption process for PFOS using Fe_3O_4@Au@Apt enrichment probes.

To obtain the Fe_3O_4@Au@Apt probe with high adsorption-desorption efficiency for PFOS, key factors influencing the adsorption and the desorption process were investigated. First, we investigated the adsorption efficiency of the Fe_3O_4@Au@Apt probes towards PFOS over a binding time range from 5 to 25 min. As shown in Fig. 3.9a, the adsorption efficiency increased with prolonged contact time and essentially reached a plateau at 15 min, achieving an adsorption efficiency of 95%. This high adsorption efficiency is mainly attributed to the strong specific affinity between PFOS and its aptamer, which enables rapid binding within a short period [7]. Therefore, an adsorption time of 15 min was selected as optimal for subsequent experiments to achieve rapid and efficient enrichment of the target. Then we examined the desorption efficiency of the PFOS-loaded Fe_3O_4@Au@Apt probes at different desorption times under 70 °C. The results (Fig. 3.9b) showed that the desorption efficiency reached a maximum of 95% within 6 min and remained stable thereafter, which is attributable to the strong disruption of non-covalent interactions in the aptamer/PFOS complex at elevated temperature. Accordingly, a desorption time of 6 min was adopted in all following experiments. Under these optimized conditions, we then investigated whether this magnetic enrichment probe could improve the analytical performance of PTS biosensor. The Fe_3O_4@Au@Apt probe was introduced to 40 mL of different concentrations of PFOS solution (nM level) for 15 min adsorption. After magnetic

2026 S.-T. Yau High School Science Award
仅用于2026丘成桐中学科学奖论文公示

separation, the PFOS-loaded probes were transferred into 40 μL of ultrapure water and heated at 70 °C for 6 min, respectively. Then, the obtained desorption supernatant was detected by PTS sensor. As shown in (Fig. 3.9c), a good linear relationship was observed between the T line intensity and initial PFOS concentration over the range of 10-400 nM, with a linear equation of y = 2109.91 + 11.48 x (where y is the T line intensity and x is the initial PFOS concentration in nM). Moreover, a visible T line signal appeared at a low initial PFOS concentration of 10 nM (~5 ppb), representing a 1000-fold improvement in sensitivity over the non-enrichment PTS sensor.

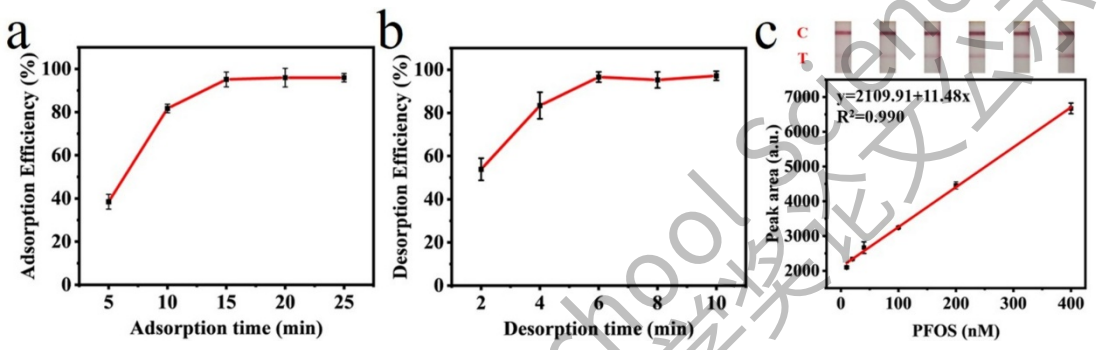


Figure 3.9. (a) Effect of adsorption time on adsorption efficiency. (b) Effect of desorption time on desorption efficiency. (c) the linear correlation between the T line signal and the PFOS concentration (10-400 nM) after 1000-fold enrichment.

3.4. Integrated Detection of Environmental Pollutants via Enrichment-PTS-Microfluidic Chip Sensor

A double-layer PMMA microfluidic chip (80 mm × 100 mm) containing three parallel serpentine channels (Fig. 1) was also fabricated to further improve the practicability. The three channels were designed for negative control, PFOS sample, and positive control, respectively. After each run, the chip is reused by removing the used PTS, injecting deionized water and air for cleaning, drying, and inserting a fresh PTS for the next measurement. The sealing, fluidic performance, and integrated detection capability of the chip were validated using dye tracing and standard analyte tests. As shown in Fig. 3.10a, rhodamine B (pink) and fluorescein sodium (yellow) were injected into two inlets of a serpentine channel. They mixed homogeneously (orange) in the reaction chamber (Fig. 3.10b). The mixture flowed to the PTS zone (Fig. 3.10c and d). After that, the capillary action drove the liquid to infiltrate the PTS thoroughly,

2026 S.T. Yau High School Science Award
仅用于2026丘成桐中学科学奖公示

as the control line appeared clearly (Fig. 3.10e). The same behavior was observed in a control channel with ultrapure water (Fig. 3.10f), confirming good sealing, no leakage or blockage, and stable fluid control.

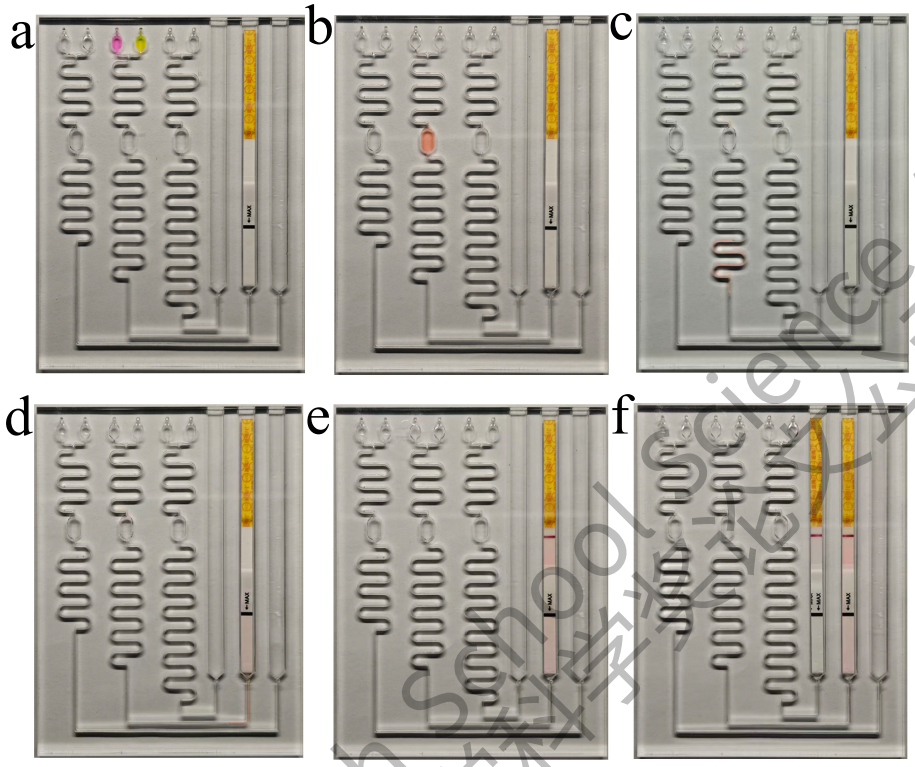


Figure 3.10. (a) Rhodamine B (pink) and fluorescein sodium (yellow) solutions were added to the two loading wells. (b) The two streams mix thoroughly in the reaction chamber, forming an orange mixture. (c) The mixture continues advancing along the channel. (d) The mixture finally reaches the PTS detection zone. (e) Driven by capillary action, the PTS absorbs the liquid and displays a clear control line. (f) The left serpentine channel, loaded with ultrapure water as a control.

The developed microfluidic chip was then used to simplify the operation of magnetic enrichment probe-integrated PTS sensor for the detection of PFOS in three real samples and one artificially spiked sample. The three channels (from left to right) were designated as the negative control (binding buffer), the test sample, and the positive control (PFOS standard solution). The negative and positive controls were used to rule out matrix interferences and assure the proper functioning of PTS biosensor. For the real-sample validation, water was collected from the Yellow River at three sections (Fig. 3.11a and 3.11b), namely Lanzhou (upstream), Zhengzhou (midstream), and Jinan (downstream). After a 1000-fold enrichment, no visible test line appeared for all three

2026 S.T. Yau High School Science Award
仅用于2026丘成桐中学科学奖公示

samples (Fig. 3.11c), indicating that the PFOS concentrations were either below the detection limit or absent. In contrast, for the artificial sample spiked with 25 ppb PFOS, a distinct test line signal was observed in the PFOS channel (Fig. 3.11d), corresponding to a detected concentration of 21 $ng \cdot L^{-1}$ and a recovery of 84%. These findings demonstrate the reliability and practical potential of the enrichment-PTS-microfluidic chip sensor for PFOS detection.

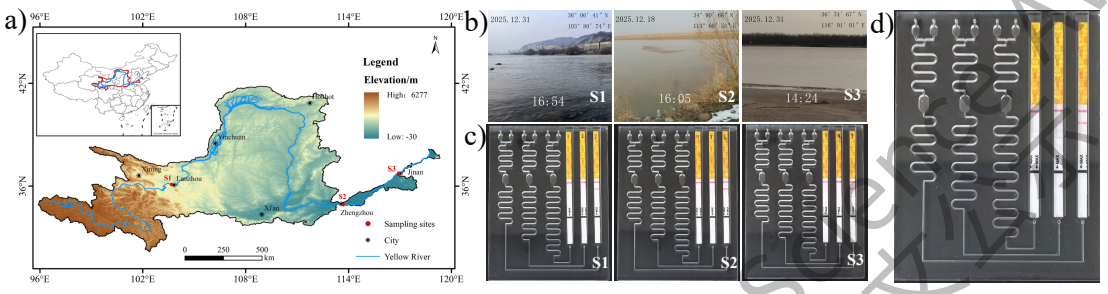


Figure 3.11. (a) Map of the Yellow River water sampling sites. (b) On-site photographs of the sampling sites. (c) PTS detection results of the Yellow River water samples after 1000-fold enrichment. (d) PTS detection results of the artificial sample after 1000-fold enrichment.

4. Conclusions

In conclusion, this study developed a PTS method for rapid and sensitive PFOS detection based on Fe_3O_4@Au@cDNA@Apt recognition probes and a signal transduction strategy that regulates hCG immunoactivity. PFOS induces the release of aptamer from the recognition probe, and the released aptamer chelates Zr^{4+}, thereby inhibiting the binding of Zr^{4+} to hCG and generating a detectable signal. Mechanistic investigation revealed that Zr^{4+} inhibits hCG immunoactivity by disrupting its conformation, while DNA competitively binds to Zr^{4+} to inhibit this disruption. To enhance sensitivity, Fe_3O_4@Au@Apt enrichment probes were further integrated, achieving a 1000-fold enrichment of PFOS. The resulting enrichment-PTS sensor enabled PFOS to be quantified to a limit of 10 nM (~5 ppb) with a linear range of 10-400 nM. Eventually, a portable microfluidic chip was further constructed to integrate the developed PTS method, achieving effective PFOS detection in real water samples. The developed PTS strategy not only provides a facile and practical tool for PFOS analysis, but also paves a new avenue for the design of non-ssDNA-hCG conjugation-based signal conversion in PTS sensing.

2026 S.T. Yau High School Science Award
仅用于2026丘成桐中学科学奖论文公示

Acknowledgments

Looking back at the past 18 months, I would like to express my sincere gratitude towards all my mentors and teachers for strongly supporting me during the exploration and research process. It is their warm companion and selfless help that together enable me to dive deeper in chemistry related fields and further understand what real research means.

I wish to first acknowledge Professor Rongbin Song and Professor Zhaohui Li at Zhengzhou University for providing me the opportunity to conduct research based on my interests. Prof. Song and Prof. Li have fully respected my interests and gave useful suggestions on choosing my research topic. I am always fascinated by the beauty of nature and especially aquatic systems such as lakes and rills. One day during my chemistry class at school, my chemistry teacher talked a bit about PFAS (also known as “forever chemicals”) and their potential risks for human health when she was explaining the extraordinary stability of carbon-fluorine bonds. I was really curious about these highly persistent substances and I searched more online afterschool, and that was when I found that PFAS, especially PFOS, may present in our daily drinking water and pose several health threats and environmental problems. Nevertheless, literatures showed that previous detection methods for PFOS are either too expensive or time-consuming, so I wanted to find a more cost-effective and rapid testing strategy. After cold-emailing, Prof. Song and Prof. Li kindly agreed to let me join their research group, and they discussed the research topic with me and gave many helpful suggestions on various research orientations that really benefited me a lot.

I would also like to thank Prof. Song and Prof. Li for giving me comprehensive guidance on the whole research process, guiding and helping me to select the suitable aptamer and design the microfluidic chip, as well as the advice they have given to help me revise my independently-written research paper. During the research process, Prof. Song also helped me adjust the experimental protocols, and always discussed with me

2026 S.-T. Yau High School Science Award
仅用于2026丘成桐中学科学奖公示

about the questions I raised after reading literatures or facing problems in experiments.

Many thanks must also go to post-graduate student Mintian Liang and Chuangyi Chi, and senior undergrad Shiyu Wang. Miss Wang had kindly guided me at the initial stage of my experiments from laboratory safety to lab reports. I am equally thankful to Mr. Liang for guiding and supporting me whether during the probe synthesis or some data analysis. Due to the required experimental durations, sometimes we didn't have time for lunch and dinner, but he always stayed for kind companion. I would also like to thank Mr. Chi for his guidance and supports during the enrichment experiments. All of their guidance and advice were so beneficial that I really learned a lot from them.

Finally, I want to acknowledge my school chemistry teacher for leading me into the amazing chemistry and science fields, and greatly motivating my interests towards on-going science and research. My gratitude also goes to my homeroom teacher, Ms. Xuexiang Xu, who has always been encouraging and supporting me during school.

For demonstrating the use of AI, I have independently written up the whole paper and graphed the illustrations (All the experimental figures or results were plotted and graphed based on raw data, with no use of AI included. Also, some schematic diagrams such as Fig.1.1 was conducted using Powerpoint, Canvas, and BioRender with no use of AI). However, I sought help from Gemini (an AI model) for optimizing figure 1.2 (a schematic illustration). I first used Powerpoint to graph the overall structure of the lateral flow assay, and then I sent it to Gemini for adjusting the colors and tri-dimensional structure. After that, I used Powerpoint again to add corresponding captions by myself.

2026 S. T. Yau High School Science Award
仅用于2026丘成桐中学科学奖论文公示

References

1. Liou, J.S.C.; Szostek, B.; Derito, C.M.; Madsen, E.L., Investigating the biodegradability of perfluorooctanoic acid, *Chemosphere*, 2010, *80*, 176-183.

2. Prevedouros, K.; Cousins, I.T.; Buck, R.C; Korzeniowski, S.H., Sources, fate and transport of perfluorocarboxylates, *Environ. Sci. Technol.*, 2006, *40*, 32-44.

3. Chen, F.Y.; Zhou, Y.; Wang, L.P.; Wang, P.F.; Wang, T.Y.; Ravindran, B.; Mishra, S.; Chen, S.H.; Cui, X.M.; Yang, Y.; Zhang, W.P., Elucidating the degradation mechanisms of perfluorooctanoic acid and perfluorooctane sulfonate in various environmental matrices: a review of green degradation pathways, *Environ. Geochem. Health*, 2024, *46*, 349.

4. Sunderland, E.M.; Hu, X.D.C.; Dassuncao, C.; Tpkranov, A.K.; Wagner, C.C.; Allen, J.G., A review of the pathways of human exposure to poly-and perfluoroalkyl substances (PFASs) and present understanding of health effects, *J. Exposure Sci. Environ. Epidemiol.*, 2019, *29*, 131-147.

5. Ahrens L, Bundschuh M., Fate and effects of poly- and perfluoroalkyl substances in the aquatic environment: A review, *Environ. Toxicol. Chem.*, 2014, *33*, 1921-1929.

6. Van der veen, I.; Fiedler, H.; de Boer, J., Assessment of the per- and polyfluoroalkyl substances analysis under the Stockholm Convention-2018/2019, *Chemosphere*, 2023, *313*, 137549.

7. Sun, X.F., High-resolution mass spectrometry analysis of legacy and emerging PFAS in oilfield environments: Occurrence, source, and toxicity assessment, *Toxics*, 2026, *14*, 116

8. Cao, S.M.X.; Wang, S.Q.; Zhou, C.X.; Yang, F.; Xia, H.; Xu, F.J.; Li, X.W.; Lan, T.; Li, M.T., Plasma-liquid interfacial F/OH exchange drives PFAS defluorination in a piezoelectric direct discharge system, *ACS Sustainable Chem. Eng.*, 2026, *14*, 8919-8930.

9. Martínez-Pérez-Cejuela, H.; Williams, M.L.; Mcleod, C.; Gionfriddo, E., Effective preconcentration of volatile per- and polyfluoroalkyl substances from gas and aqueous phase via solid phase microextraction, *Anal. Chim. Acta*, 2025, *1345*, 343746.

2026 S.-T. Yau High School Science Award 仅用于2026丘成桐中学科学奖公示

10. Ranaweera, R.; Ghafari, C.; Luo, L., Bubble-nucleation-based method for the selective and sensitive electrochemical detection of surfactants, *Anal. Chem.*, 2019, *91*, 7744-7748.

11. Cao, Y.; Lee, C.P.; Davis, E.T.J.; Si, W.M.; Wang, F.G.; Trimpin, S.; Luo, L., 1000-fold preconcentration of per- and polyfluorinated alkyl substances within 10 minutes via electrochemical aerosol formation, *Anal. Chem.*, 2019, *91*, 14352-14358.

12. Chen, G.S.; Zhou, X.; Wu, L.X.; Jia, S.Y.; Shan, B.; Zheng, C.Y.; Tian, Y.; Ma, J.P.; Gu, C.T., Conjugated polymer nanoparticle-enhanced molecularly imprinted poly(*o*-phenylenediamine) electrochemical sensors for selective, sensitive and rapid detection of trace perfluorooctanesulfonate, *J. Mater. Chem. A*, 2025, *13*, 22365-22374.

13. Wan, W.Q.; Zhao, H.L.; Qian, B.; Lan, M.B., A molecularly imprinted electrochemical sensor based on nitrogen-doped graphene oxide nanoribbons and Au-Pt bimetallic nanoparticles for ultrasensitive detection of perfluorooctane sulfonate (PFOS) in aqueous medium, *Microchem. J.*, 2025, *215*, 114256.

14. Khan, R.; Uygun, Z.O.; Andreescu, D.; Andreescu, S., Sensitive detection of perfluoroalkyl substances using MXene-AgNP-based electrochemical sensors, *ACS Sens.*, 2024, *9*, 3403-3412.

15. Yao, P.L.; Zhao, W.H.; Zhao, D.D.; Wang, Q.; Chen, M., Synthesis and imaging applications of a novel fluorescent probe for one-step dual detection of perfluorooctanoic acid and perfluorooctane sulfonate, *Chin. J. Syn. Chem.*, 2025, *33*, 920-931.

16. Cheng, Z.; Dong, H.C.; Liang, J.M.; Zhang, F.; Chen, X.P.; Du, L.L.; Tan, K.J.L., Highly selective fluorescent visual detection of perfluorooctane sulfonate via blue fluorescent carbon dots and berberine chloride hydrate, *Spectrochim. Acta, Part A*, 2019, *207*, 262-269.

17. Jiao, Z.; Li, J.W.; Mo, L.J.; Liang, J.M.; Fan, H.B., A molecularly imprinted chitosan doped with carbon quantum dots for fluorometric determination of perfluorooctane sulfonate, *Microchim. Acta*, 2018, *185*, 473.

18. Wang, Y.F.; Zhu, H.Y., Detection of PFOS and copper (II) ions based on complexation induced fluorescence quenching of porphyrin molecules, *Anal. Methods*,

2026 S.-T. Yau High School Science Award 仅用于2026丘成桐中学科学奖论文公示

2014, *6*, 2379-2383.

19. Liu, Q.; Huang, A.Z.; Wang, N.; Zheng, G.; Zhu, L.H., Rapid fluorometric determination of perfluorooctanoic acid by its quenching effect on the fluorescence of quantum dots, *J. Lumin.*, 2015, *161*, 374-381.

20. Li, J.; Zhang, C.Y.; Yin, M.Y.; Zhang, Z.; Chen, Y.J.; Deng, L.; Wang, S., Surfactant-sensitized covalent organic frameworks-functionalized lanthanide-doped nanocrystals: an ultrasensitive sensing platform for perfluorooctane sulfonate, *ACS Omega*, 2019, *4*, 15947-15955.

21. Xu, Y.Y.; Wang, T.; Chen, Z.; Jin, L.; Wu, Z.Z.; Yan, J.Q.; Zhao, X.N.; Cai, L.; Deng, Y.; Guo, Y.; Li, S.; He, N.Y., The point-of-care-testing of nucleic acids by chip, cartridge and paper sensors, *Chin. Chem. Lett.*, 2021, *32*, 3675-3686.

22. Zheng, S.; Xia, X.; Tian, B.S.; Xu, C.Y.; Zhang, T.; Wang, S.; Wang, C.W.; Gu, B., Dual-color MoS_2@QD nanosheets mediated dual-mode lateral flow immunoassay for flexible and ultrasensitive detection of multiple drug residues, *Sens. Actuators, B*, 2024, *403*, 135142.

23. Wu, P.C.; Song, J.R.; Sun, C.X.; Zuo, W.C.; Dai, J.J.; Ju, Y.M., Recent advances of lateral flow immunoassay for bacterial detection: capture-antibody-independent strategies and high-sensitivity detection technologies, *Trends Anal. Chem.*, 2023, *166*, 117203.

24. Meng R.Y.; Ji, J.N.; Zhao, Y.; Zhang, Y.F.; Wang, X.; Wang, Z.Z., Research advances in the clinical application of lateral flow assay-based point-of-care testing. *J. Chongqing Med. Univ.*, 2025, *50*, 1710-1716.

25. Jiang, H.; Deng, Y.L.; Lv, X.F.; Liu, Y.; Li, A.Y.; Li, X.Q., New sensing methods using commercially available products: Based on PGM and PTS, *Biosens. Bioelectron.*, 2025, *267*, 116836.

26. Du, Y.; Pothukuchy, A.; Gollihar, J.D.; Nourani, A.; Li, B.L., Ellington, A.D.; Coupling sensitive nucleic acid amplification with commercial pregnancy test strips, *Angew. Chem., Int. Ed.*, 2017, *56*, 992-996.

27. Qi, L.J.; Yang, M.T.; Chang, D.R.; Zhao, W.J.; Zhang, S.C.; Du, Y.; Li, Y.F., A DNA nanoflower-assisted separation-free nucleic acid detection platform with a commercial

2026 S.T. Yau High School Science Award
仅用于2026丘成桐中学科学奖论文公示

pregnancy test strip, *Angew. Chem., Int. Ed.*, 2021*, 60,* 24823-24827.

28. Yang, M.T.; Tang, Y.D.; Qi, L.J.; Zhang, S.C.; Liu, Y.C.; Lu, B.Y.; Yu, J.X.; Zhu, K.; Li, B.L.; Du, Y., SARS-CoV-2 point of care (POC) diagnosis based on commercial pregnancy test strips and a palm-size microfluidic device, *Anal. Chem.*, 2021, *93*, 11956-11964.

29. Jiang, H.; Qian, C.; Deng, Y.L.; Lv, X.F.; Liu, Y.; Li, A.Y.; Li, X.Q., Novel multimode assay based on asymmetrically competitive CRISPR and Raman barcode spectra for multiple hepatocellular carcinoma biomarkers detection, *Anal. Chem.*, 2024, *96*, 20004-20014.

30. Tang, Y.D.; Qi, L.J.; Liu, Y.C.; Guo, L.L.; Zhao, R.J.; Yang, M.T.; Du, Y.; Li, B.L., CLIPON: a CRISPR-enabled strategy that turns commercial pregnancy test strips into general point-of-need test devices, *Angew. Chem., Int. Ed.*, 2022, *61*, e202115907.

31. Zhang, Y.; Ma, C.B.; Yang, M.T.; Pothukuchy, A.; Du, Y., Point-of care testing of various analytes by means of a one-step competitive displacement reaction and pregnancy test strips, *Sens. Actuators, B*, 2019, *288*, 163-170.

32. Zhong, Z.T.; He, Y.F.; Tang, Y.J.; Ashraf, G; Yang, H.; Chen, W.; Liu, B.; Wang, G.P.; Zhao, Y.D., Terminal deoxynucleotidyl transferase associated with split G-quadruplex/hemin deoxyribozyme amplification detection for various contaminants in milk based on pregnancy test strip platform, *Biosens. Bioelectron.*, 2022, *216*, 114644.

33. Deng, Z.Q.; Wang, S.Y.; Song, H.J.; Liu, R.; Lv, Y., Bisphenol a monitoring by commercial pregnancy test strips transformed by DNA walking machine, *Food Chem.*, 2025, *464*, 141775.

34. He, Q.; Su, H.; Jiang, H.X.; Liu, L.S.; Zhang, S.S., Responsive release of guest aqueous droplet in liquid crystal droplet assists the detection of organophosphorus using commercial pregnancy test strip, *Sens. Actuators, B*, 2025, *423*, 136777.

35. Park, H.J.; Kim, Y.; Lee, K.W.; Gwon, M.; Yoon, H.C.; Yoo, T.H., Coupling hCG-based protease sensors with a commercial pregnancy test strip for simple analyses of protease activities, *Biosens. Bioelectron.*, 2023, *235*, 115364.

36. Jia, Z.Z.; Zhang, Y.J.; Zhang, C.Y.; Wei, X.Y.; Zhang, M.Z., Biosensing intestinal alkaline phosphatase by pregnancy test strips based on target-triggered CRISPR-

2026 S. F. Yau High School Science Award
仅用于2026丘成桐中学科学奖论文公示

Cas12a activity to monitor intestinal inflammation, *Anal. Chem.*, 2023, *95*, 14111-14118.

37. Zhong, Z.T.; Song, L.B.; He, Y.F.; Zhang, B.; Chen, W.; Liu, B.; Zhao, Y.D., Detection of multiple mycotoxins based on catalytic hairpin assembly coupled with pregnancy test strip, *Sens. Actuators, B*, 2022, *350*, 130911.

38. Jia, Z.Z.; Wei, W.; Tu, K.S.; Fang, B.Y.; Zhang, M.Z.; Shi, L.L., Point-of-care monitoring of dry eye disease using lysozyme in tear based on commercial pregnancy test strips, *Sens. Actuators, B,* 2023, *378*, 133179.

39. Zhong, Z.T.; Ashraf, G.; Chen, W.; Liu, B.; Wang, G.P.; Zhao, YD., Detection of matrix metalloproteinase-1 in human saliva based on a pregnancy test strip platform, *Anal. Chem.*, 2022, *94*, 16384-16392.

40. Deng, Z.Q.; Zhou, J.; Wang, C.Q.; Hu, J.Y.; Liu, R.; Lv, Y., Rapid and sensitive point-of-care PTS-CRISPR assay for food safety monitoring of aflatoxin B1, *Chem. Commun.*, 2023, *59*, 12011-12014.

41. Zhang, H.; Hu, X.L.; Bao, X.D.; Tu, W.; Wan, Q.W.; Yu, Z.H.; Xie, J.; Qiu, X.P.; Gu, W.; Gao, Z.L.; Wang, Y.Z.; Wang, C.X.; Luo, Y., Commercial strip-inspired one-pot CRISPR-based chip for multiplexed detection of respiratory viruses, *Small Methods,* 2025, *9*, 2400917.

42. Zhao, R.J.; Tang, Y.D.; Song, D.F.; Liu, M.; Li, B.L., CRISPR/Cas12a-responsive hydrogels for conjugation-free and universal indicator release in colorimetric detection, *Anal. Chem.*, 2023, *95*, 18522-18529.

43. Xu, W.J.; Lin, Z.X.; Kim, C.J.; Wang, Z.R.; Wang, T.Z.; Cortez-Jugo, C.; Caruso, F., Assembly and biological functions of metal-biomolecule network nanoparticles formed by metal-phosphonate coordination, *Sci. Adv.*, 2024, *10*, eads9542.

44. Zhang, H.; Liu, Y.; Zhang, R.; Liu, R.; Chen, Y., Binding mode investigations on the interaction of lead(II) acetate with human chorionic gonadotropin, *J. Phys. Chem. B*, 2014, *118*, 9644-9650.

45. Li, C.C.; Wang, Y.A.; Zhang, R.; Zhang, Y.; Chang, Y.Y.; Zhang, Z.J.; Yuan, H; Liu, R.D.; Li, J.X.; Liu, M., Advances in aptamer-based sensors for environmental small-molecule pollutant detection, *Trends Anal. Chem.*, 2026, *203*, 119018.

2026 S.T. Yau High School Science Award
仅用于2026丘成桐中学科学奖论文公示

46. Park, J.; Kim, D.; Kim, D.; Jung, J.; Zoh, K.D.; Lee, C.; Choi, Y.; Choe, J.K., Development of an aptamer-based qPCR method for the selective and rapid picomolar-level detection of perfluorooctanesulfonic acid in water, *Environ. Sci. Technol.*, 2025, *59*, 17247-17257.47.

47. Liu, J.; Sun, Z.; Deng, Y.; Zou, Y.; Li, C.; Guo, X.; Xiong, L.; Gao, Y.; Li, F.; Zhao, D., Highly water-dispersible biocompatible magnetite particles with low cytotoxicity stabilized by citrate groups, *Angew. Chem., Int. Ed.*, 2009, *48*, 5875-5879.

48. Wang, Y.X.; Sun, J.L.; Wang, C.; Qu, L.; Zhang, L.; Li, Y.P.; Song, R.B.; Li, Z.H., Target-responsive regulation of bacteria-surface magnetic element for self-powered analysis of Aflatoxin B1 in microbial fuel cell, *Anal. Chem.*, 2025, *97*, 8484-8490.

49. Song, R.B.; Zhao, C.E.; Jiang, L.P.; Abdel-Halim, E.S.; Zhang, J.R.; Zhu, J.J., Bacteria-affinity 3D macroporous graphene/MWCNTs/Fe_3O_4 foams for high-performance microbial fuel cells, *ACS Appl. Mater. Interfaces,* 2016, *8*, 16170-16177.

50. Jiang, Y.J.; Li, P.P.; Wang, Y.Y.; Jiang, LP.; Song, R.B.; Zhang, J.R.; Zhu, J.J., Trifunctional modification of individual bacterial cells for magnet-assisted bioanodes with high performance in microbial fuel cells, *J. Mater. Chem. A*, 2020, *8*, 24515-24523.

51. Yu, S.; Zhou, Y.; Sun, Y.; Wu, S.J.; Xu, T.T.; Chang, Y.C.; Bi, S.; Jiang, L.P.; Zhu, J.J., Endogenous mRNA triggered DNA-Au nanomachine for in situ imaging and targeted multimodal synergistic cancer therapy, *Angew. Chem., Int. Ed.*, 2021, *60*: 5948-5958.

52. Qi, X.; Xu, D.X.; Zhu, J.J.; Wang, S.J.; Peng, J.W.; Gao, W.; Cao, Y.P., Studying the interaction mechanism between bovine serum albumin and lutein dipalmitate: Multi-spectroscopic and molecular docking techniques, *Food Hydrocolloids*, 2021, *113,* 106513.

53. Zhang, H.; Liu, Y.; Zhang, R.; Liu, R.T.; Chen, Y.D., Binding mode investigations on the interaction of lead(ii) acetate with human chorionic gonadotropin, *J. Phys. Chem. B*, 2014, *118*, 9644-9650.

2026 S.T. Yau High School Science Award
仅用于2026丘成桐中学科学奖论文公示